Force Estimation and Shape Reconstruction of Soft Robots in Contact with Fluid Flow: theory and experiment

Reza Khoshbakht

A Thesis

in

The Department

of

Mechanical, Industrial and Aerospace Engineering

Presented in Partial Fulfillment of the Requirements

For the Degree of Master of Applied Science (Mechanical Engineering)

Concordia University

Montréal, Québec, Canada

August 2023

Concordia University

School of Graduate Studies

This is to certify that the thesis prepared

By: **Reza Khoshbakht**

Entitled: **Force Estimation and Shape Reconstruction of Soft Robots in Contact with Fluid Flow: theory and experiment**

and submitted in partial fulfillment of the requirements for the degree of

Master of Applied Science (Mechanical Engineering)

complies with the regulations of this University and meets the accepted standards with respect to originality and quality.

Signed by the final examining committee:

_____ Dr. Marius Paraschivoiu, Chair and Internal Examiner

_____ Dr. Hang Xu, Internal Examiner

_____ Dr. Javad Dargahi, Co-Supervisor

_____ Dr. Mojtaba Kheiri, Co-Supervisor

Approved by _____

Dr. Martin D. Pugh, Chair

Department of Mechanical, Industrial and Aerospace Engineering

_____ _____

18/09/2023

Dr. Mourad Debbabi, Dean

Gina Cody School of Engineering and Computer Science

Abstract

Force Estimation and Shape Reconstruction of Soft Robots in Contact with Fluid Flow: theory and experiment

Reza Khoshbakht

This thesis explores two significant aspects of robotic-assisted surgeries. The first part focuses on a procedure called Robotic Catheter Ablation, which utilizes robots to treat a heart condition known as Atrial fibrillation. The procedure aims to determine the contact force at the robot's tip without the direct use of a force sensor, ensuring proper contact with the patient's heart. Recent findings have highlighted the importance of considering blood flow within the heart, as it can significantly impact the procedure's success, often neglected in similar studies. This research examines the experimental effects of blood flow on the movement of soft robots and demonstrates how disregarding this effect can lead to less effective treatments. Simultaneously, this study focuses on enhancing soft robots, introducing a method for determining their shape when subjected to varying forces, similar to the way blood flow affects them. This is accomplished through mathematical modeling, employing Euler-Bernoulli beam theory and cubic Bézier curves. The model's accuracy is confirmed through finite element method testing. Additionally, the research goes beyond shape prediction by including an approach known as Bayesian neural network (BNN). This BNN significantly improves our ability to update information rapidly, valuable for various real-time applications. In the final part of this research, applying the reshaped dataset from the shape reconstruction phase, it is demonstrated that the results obtained from the

mathematical model can estimate forces using a new neural network, validated through experimentation. The proposed model holds potential for use in different fields of soft robotics, crucial for surgical procedures.

Acknowledgments

In loving memory of my hero, my idol, my leader, my commander, my teacher, my father who lost his battle with COVID-19, whose irreparable absence casts an everlasting shadow over this crucial harvesting moment. This is a testament to the values and strength you instilled in me.

I want to express my sincere thanks to those who have played a pivotal role in bringing this thesis to fruition:

To my dear cherished jewel, my beloved wife, Arefeh, for her unending patience, encouragement, and understanding during the challenges of this academic pursuit, and to my endless source of kindness and strength, my mother Zohreh, for her indefatigable unhesitating belief in me, to two pillars of support, my two sisters Neda and Roza for their constant love, encouragement, and to my lovely nephew Kian and his gentlemen father Hadi. I literally find joy in your presence beside me.

A special thank you to Dr. Dargahi, Dr. Kheiri, and Dr. Hooshiar for their exceptional guidance, mentorship, and unwavering support throughout my academic journey. Your expertise, insights, and dedication have profoundly impacted my life and educational pursuits.

I owe a debt of gratitude to my friends and colleagues, Mojtaba, Sobhan, Shahrzad, Amir, Hamid, Amar, and Farzad, for their invaluable contributions and support during my research. Your willingness to share knowledge, ideas, and insights has been immeasurable.

Lastly, my appreciation goes to all those who have supported me in various ways on this academic journey. Your encouragement and assistance have played a pivotal role in helping me reach this significant milestone. To each and every one of you, I extend my heartfelt thanks for being an integral part of my journey.

Reza

August 2023

Contents

List of Figures

List of Tables

Chapter 1

Introduction

1.1 Background

1.1.1 Minimally Invasive Surgery

Minimally invasive surgery (MIS) is a surgical approach that aims to minimize patient trauma and promote faster recovery by using small incisions and specialized instruments (see Figure 1.1). This technique has gained significant attention and popularity in various surgical fields due to its numerous advantages over traditional open surgery. MIS offers reduced postoperative pain, shorter hospital stays, decreased blood loss, minimized potential in-hospital contamination, and improved cosmetic outcomes [46]. Thanks to its numerous benefits, it proves highly valuable across a diverse array of surgical procedures. Moreover, these advancements are progressively asserting their dominance in various fields incrementally. As an illustrative example, Figure 1.2 showcases the substantial rise in the utilization of MIS (represented by the green line), replacing traditional open surgery (indicated by the blue line) for Appendectomy procedures, which involves the removal of an inflamed or infected appendix in the state of Maryland, U.S [61].

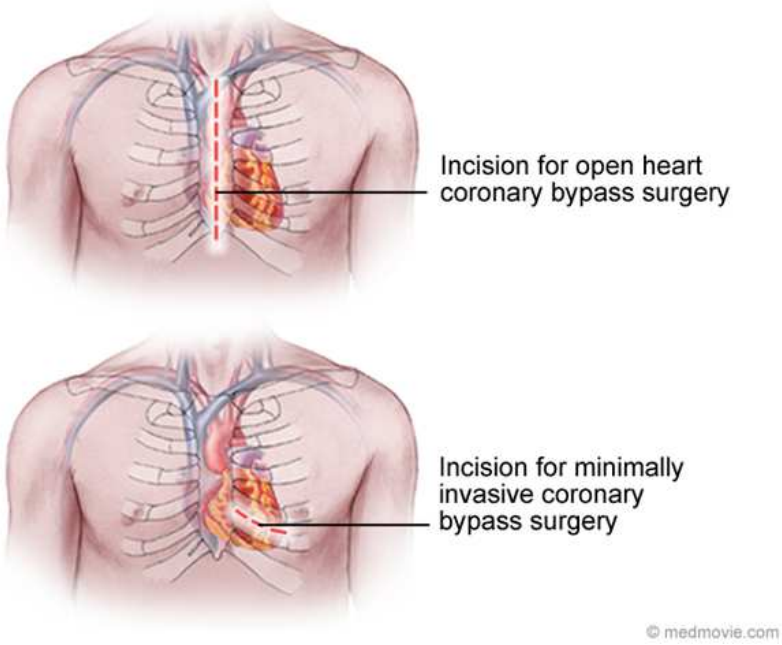

Figure 1.1: A comparison of incision sizes between traditional open heart surgery (top) and Minimally Invasive Surgery (bottom) [2]

MIS has modernized the field of cardiovascular disease treatments, offering improved diagnostic imaging techniques [79], blood-resistant surgical glues [69], minimally invasive surgical approaches [6], digital medicine applications [132], and the use of shape memory alloys in surgical devices [108]. These advancements in MIS have significantly contributed to the diagnosis, treatment, and management of cardiovascular diseases, leading to improved patient treatment outcomes. In the field of plastic surgery, MIS techniques have been widely used for procedures such as double eyelid surgery. A study comparing different double eyelid surgical techniques found that the minimally invasive 3-point subcutaneous tunnel method resulted in milder postoperative swelling and congestion compared to other approaches [130]. This highlights the benefits of MIS in achieving desired aesthetic outcomes with minimal tissue trauma. MIS has also made significant advancements in the field of hernia repair. Robotic techniques have been developed to address complex abdominal wall hernias, offering

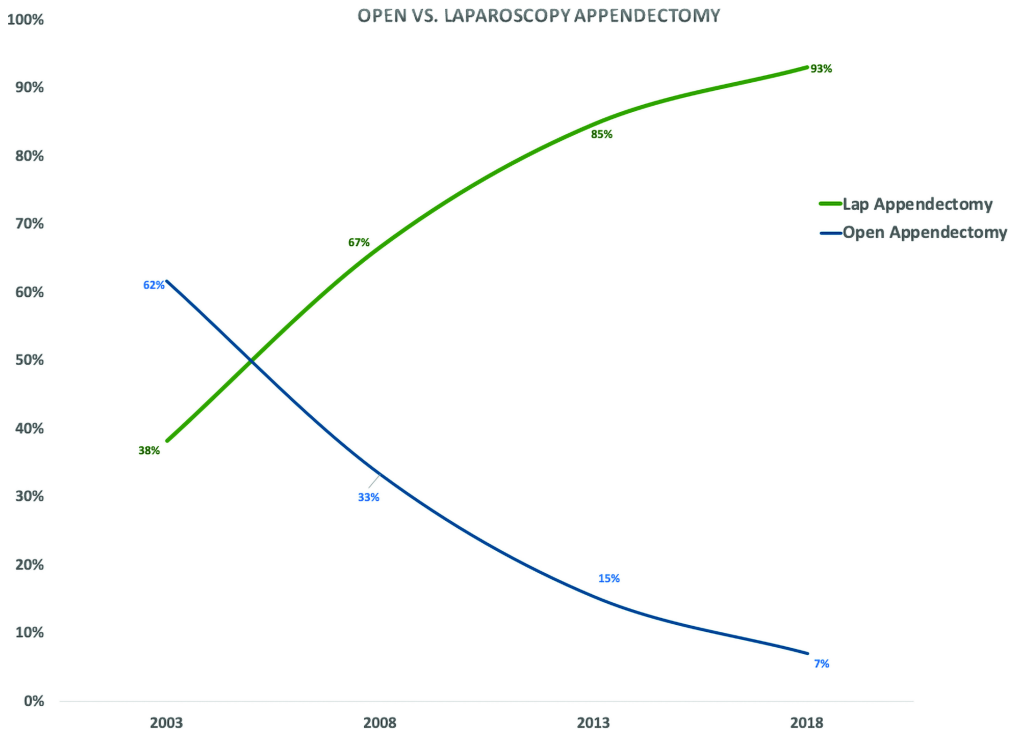

Figure 1.2: The remarkable surge in Minimally Invasive Surgery and its gradual substitution for Open Procedures [61].

a robust repair with minimal complications. Robotic hernia repair has shown comparable results to standard laparoscopy, with some studies even demonstrating improved outcomes such as shorter hospital stays [38]. In the field of spine surgery, MIS techniques have been developed to minimize surgical morbidity. Minimally invasive spine surgery (MISS) aims to reduce operative time, blood loss, tissue handling, and neural structure manipulation, resulting in improved patient outcomes. Studies have shown that the invasiveness of spine surgery is correlated with operative time and blood loss, highlighting the importance of minimizing these factors [23].

The application of MIS techniques has also expanded to other areas, such as liver surgery and implant therapy. Robotic liver surgery has experienced significant growth, offering

additional technical advantages over traditional laparoscopic surgery [10]. Minimally invasive implant therapy has shown favorable clinical effects and aesthetic outcomes in the treatment of dentition defects [73]. It also has transformed orthopedics with various applications, leading to improved techniques and patient outcomes. Key applications include Endoscopic Extreme Transforaminal Lumbar Interbody Fusion (eXTLIF) [41], Minimally Invasive Plate Osteosynthesis (MIPO) for supracondylar humerus fractures [84], Minimally Invasive Transforaminal Lumbar Interbody Fusion (MI-TLIF) for degenerative spine disease [29], SuperPath Technique for Total Hip Arthroplasty (THA) which resulted in smaller scars and decreased the risk of infection [36], and Minimally Invasive Surgery for Hallux Valgus as examples of modified surgical methods that improve clinical efficacy [18, 49].

Overall, MIS has revolutionized various surgical fields by offering less invasive approaches with numerous benefits for patients. The advancements in robotic technology have further enhanced the capabilities of MIS, allowing for precise and dexterous surgical interventions. However, it is important to continue research and development in order to optimize and expand the applications of MIS techniques.

1.1.2 Soft robots in Minimally Invasive Surgeries

A soft robot is a class of robotic systems constructed using flexible and compliant materials, such as elastomers or soft plastics, in contrast to conventional rigid robots. These soft robots possess the ability to bend, deform, and adapt to their surroundings, offering enhanced versatility in a wide range of applications. Drawing inspiration from the flexibility and dexterity observed in biological organisms, soft robots find utility in various domains, including medical devices, industrial automation, search and rescue missions, and exploration in challenging and unstructured environments. Due to these inherent advantages, soft robots are exceptionally well-suited for application in minimally invasive surgeries. Their

flexible and adaptable nature allows them to navigate through confined spaces and delicate anatomical structures with precision, making them valuable tools for surgeons during procedures that require minimal incisions. The types of soft robots used in MIS can be broadly categorized into the following:

1. Soft Endoscopes:

Figure 1.3: Soft Self propelled endoscopic robot [3]

A soft endoscope is a type of robotic device that is specifically designed for endoscopic applications. It is typically composed of soft deformable materials and is used for minimally invasive procedures such as medical imaging and surgery. Soft endoscopes are lightweight and can be miniaturized, making them ideal for navigating through narrow and complex anatomical structures. They often have a flexible backbone that can be manipulated remotely using tendons such as tendon-driven soft catheters or other mechanisms. The flexibility of soft endoscopes allows them to conform to the shape of the body and navigate through tight spaces, providing a high degree of dexterity. However, the flexibility of soft endoscopes also poses challenges in terms of modeling and control, especially when closed-loop control is required. The modeling of soft endoscopes can be done theoretically by modeling the behavior of the backbone [59].

2. Continuum Robots:

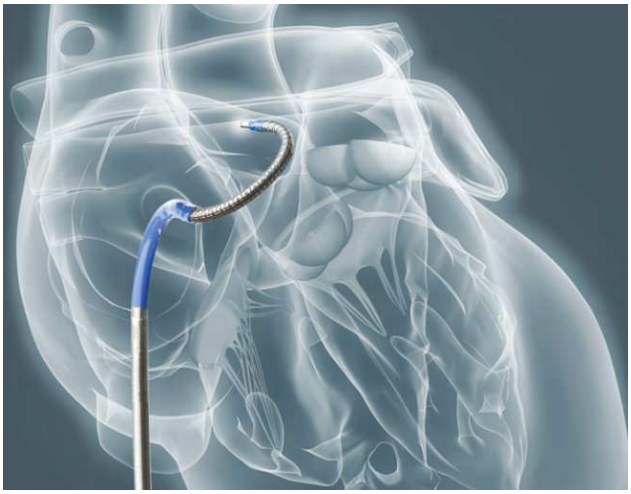

Figure 1.4: 6 Degree of freedom force sensing catheter as a type of soft continuum robot [1]

Continuum robot is a type of robotic device that is characterized by its lack of rigid linkages. Instead of rigid links and joints, continuum robots have a continuous backbone that is connected by flexible components [74]. This allows continuum robots to have a wide range of motion, shape adaptability, and compliance. The lack of rigid linkages in continuum robots makes them more suitable for tasks that require gentle stretching and bending of the robot's body, such as manipulation in chaotic environments or delicate surgical procedures. Continuum robots can be driven by various mechanisms, such as wires or cables, and can be controlled remotely [63]. The modeling of continuum robots can be challenging due to their high flexibility and the complex deformations they can undergo in response to external forces and positional constraints [27]. The main difference between a soft endoscope and a continuum robot lies in their intended applications and the specific design features that enable them to perform those applications. Soft endoscopes are designed for endoscopic procedures and are characterized by their lightweight, miniaturized, and flexible nature. Continuum robots, on the other hand, have a wide range of motion, shape adaptability,

and compliance, making them suitable for tasks that require gentle manipulation and navigation in complex environments

3. Soft Graspers and Manipulators:

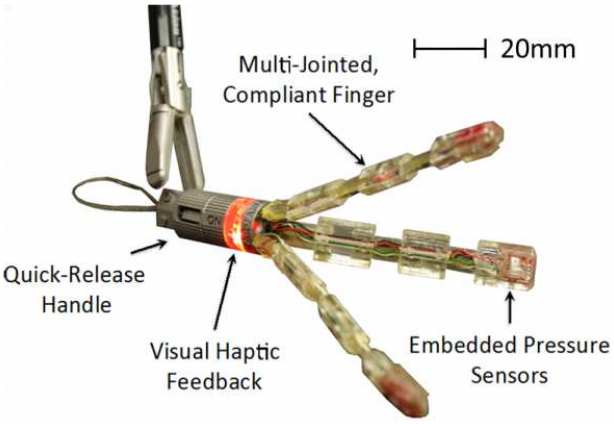

Figure 1.5: Laparoscopic soft grasper designed for pancreatic surgery, aiding in delicate tissue manipulation and hemorrhage control. [4]

Soft graspers and manipulators are a type of soft robotic devices that are designed to mimic the flexibility and adaptability of natural organisms. These devices are made of soft materials and flexible components, allowing them to deform and conform to their environment and are typically driven by pneumatic or fluidic actuators, which enable them to perform various tasks with high dexterity and precision [124]. In the context of minimally invasive surgeries, they offer several advantages over traditional rigid robotic tools. Soft manipulators can adapt their shapes to cluttered environments, making them well-suited for surgical procedures that require precise and intricate movements [105]. Soft graspers are particularly useful for handling fragile objects or delicate tissues, as their compliant nature reduces the risk of damage. Soft manipulators can also be integrated with imaging systems to provide real-time feedback and enhance surgical precision [11].

4. Soft Capsule Robots:

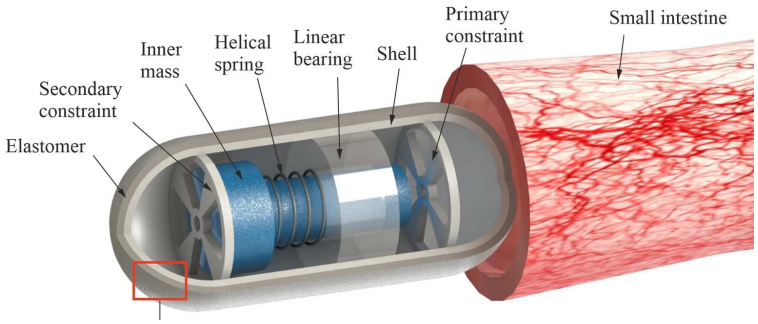

Figure 1.6: Components of elastomer coated soft capsule robot [116]

The application of soft capsule robots in minimally invasive surgery offers several advantages. Firstly, their compliance and flexibility enable them to adapt to the deformable nature of soft tissues, allowing for more precise and controlled movements [37], reducing the risk of injury to surrounding tissues [120]. Additionally, soft robots can navigate through narrow and restricted spaces, such as blood vessels or the gastrointestinal tract, which are difficult to access with conventional surgical instruments [121]. This capability opens up new possibilities for performing procedures in hard-to-reach areas of the body [65]. Soft capsule robots also have the potential to improve the accuracy and effectiveness of surgical interventions. They can be equipped with sensors and imaging technologies to provide real-time feedback and enhance the surgeon's perception of the surgical site [121].

5. Soft Sensors:

Soft Sensors play a crucial role in providing proprioceptive feedback and shape-sensing capabilities to soft robots used in minimally invasive surgeries. These sensors enable safe interaction with the human body, precise control of robot-tissue interaction, and accurate measurement of deformation and external forces [33, 121]. Their valuable force and shape control capabilities render them exceptionally useful for real-time

control during high-sensitive surgeries. These robots operate through diverse sensing techniques like stretchable fiber Bragg grating (FBG) [54] and capacitive sensing [133], enhancing their suitability for precise surgical interventions.

6. Biohybrid Soft Robots:

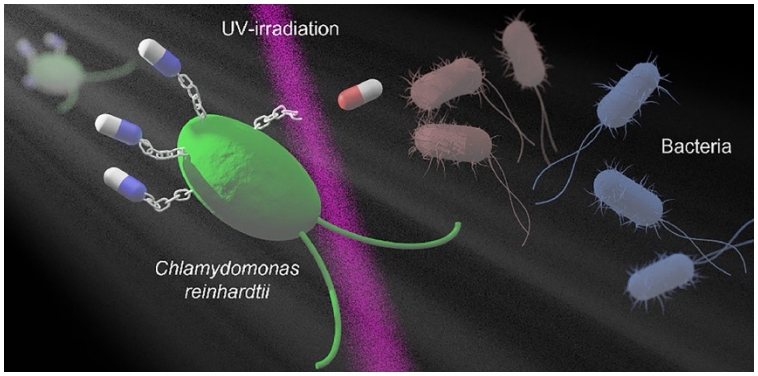

Figure 1.7: Biohybrid Soft Robot navigating for drug delivery against bacterial infections [104]

Biohybrid soft robots are a type of soft robots that incorporate biological components or materials into their design. These robots combine the advantages of soft robotics, such as flexibility and compliance, with the unique properties of biological materials, such as self-healing and responsiveness [14]. The integration of biological components allows biohybrid soft robots to mimic the complexity and functionality of living organisms, enabling them to perform tasks with greater adaptability and versatility [127]. One of the key advantages of these robots is their ability to access confined and hard-to-reach spaces in the human body non-invasively [35]. This makes them well-suited for tasks such as targeted drug delivery, where precise and localized delivery of therapeutic agents is required [127]. Biohybrid soft robots can navigate through narrow channels and maneuver in complex environments, allowing them to reach specific target sites with minimal trauma to surrounding tissues [110]. They can also be used for organ-on-a-chip applications, tissue engineering, and cell manipulation [127]. Additionally, the

adaptability of biohybrid soft robot control is crucial in minimally invasive surgeries, as the task environment conditions can vary dynamically, requiring the robot to adjust its motion and performance accordingly [35].

It should be noted that some specific models of catheters can be considered as a type of soft continuum robots, as they share similar characteristics such as flexibility and the ability to navigate through the body [77]. However, not all catheters can be classified as soft continuum robots. The term "soft continuum robot" specifically refers to a type of robot that is composed of soft materials and can undergo continuous deformation to adapt to its environment [20].

1.1.3 Robotic-Assisted Surgeries

Robotic-assisted surgeries, also known as robotic surgeries, are medical procedures where a robotic system assists the surgeon in performing surgical tasks with enhanced precision and control. These robotic systems are designed to work collaboratively with the surgeon to provide improved dexterity, stability, and visualization during the surgery. In robotic-assisted surgeries, the surgeon remains in full control of the procedure and operates the robotic system from a console. The console typically offers a 3D visualization of the surgical site and allows the surgeon to manipulate surgical instruments using hand and foot controls. The robotic system translates the surgeon's movements into precise actions, making it possible to perform intricate maneuvers and complex procedures with greater accuracy. Robotic-assisted surgeries are often performed in minimally invasive surgeries, such as laparoscopy or endoscopy.

The robotic system's smaller instruments can be inserted into the patient's body through tiny incisions or natural body openings, reducing the need for larger incisions required in traditional open surgeries. The da Vinci Surgical System is one of the most well-known

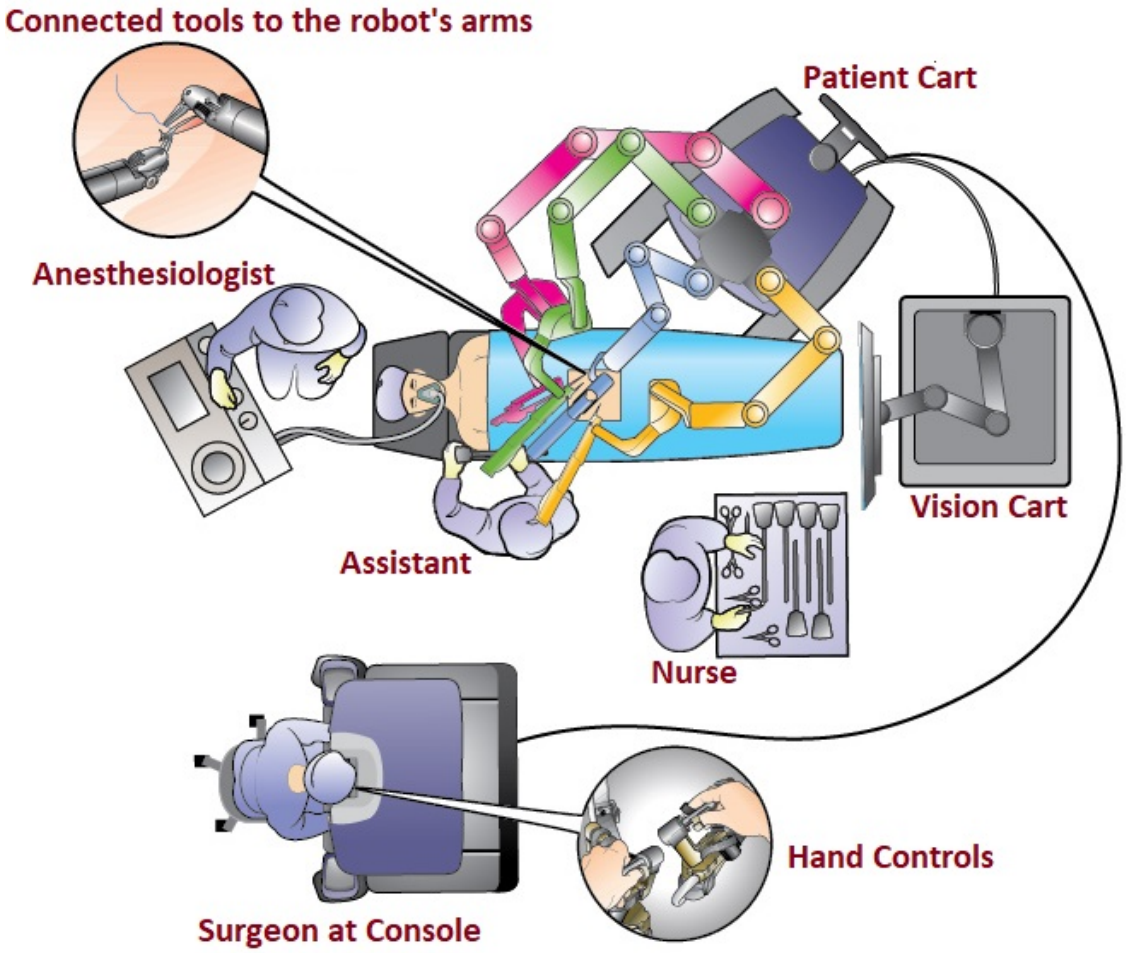

Figure 1.8: Configuration and components of a Robotic-Assisted Surgical setup, featuring the DaVinci Surgical System in an operating room [*@Intuitive Surgical, Inc.*].

examples of a robotic-assisted surgical system, widely used in various medical specialties, including urology, gynecology, general surgery, and cardiac surgery. Figure 1.8 illustrate the elements of a Da Vinci system used in robotic-assisted surgeries. Depending on the specific surgical procedure required, the tools attached to the robotic arms are customized. Through the patient's cart and hand controls, the surgeon can conduct the intervention without direct physical contact with the patient's body. These Surgical Systems offer several advantages over traditional surgery. The high-definition vision system provides a clear and magnified

view of the surgical site, allowing for precise and accurate movements [106]. The robotic arms have a greater range of motion and can perform complex maneuvers that may be difficult for human hands. The system also filters out hand tremors (i.e. shaking), further enhancing surgical precision [26]. Additionally, the system allows for a dual-console mode, which enables real-time teaching, surgical collaboration, and telementoring [106].

The success of a robotic surgery operation depends on various factors, and a combination of these elements contributes to achieving positive outcomes. Some of the key factors are the surgeon's skill and experience, teamwork, and effective communication among the surgical team. The engineering contribution to this objective is focused on enhancing robotic systems and advancing technology. The quality and capabilities of the robotic surgical system used play a significant role. State-of-the-art robotic platforms with advanced features enable precise movements and enhanced visualization, leading to better surgical outcomes.

1.1.4 Clinical Need

As previously mentioned, the surgical team requires continuous monitoring of vital signs and procedure advancement during surgery. Currently, this objective is achieved using a range of costly force sensors and high-tech medical imaging equipment, which have their own limitations. The need becomes even more critical when employing soft-robots for minimally invasive medical interventions in challenging and inaccessible fluid-filled confined areas, such as vessels, tubes, channels, and cavities, which are filled with stagnant or flowing biological fluids [95]. Patient safety remains an ongoing and critical concern, necessitating careful control over various factors to reduce the risk of unintended tissue damage and improve precision in medical procedures. This research specifically targets one crucial element that plays a significant role in meeting this imperative need for enhanced healthcare practices. The effective control and handling of robot arms and soft robots depend on several factors, with

one crucial aspect being real-time tracking of the robot's position within the patient's body. Developing a precise and cost-effective technique for this purpose can enhance accessibility to these procedures and reduce reliance on expensive medical imaging equipment, while also lowering X-ray exposure for patients. By achieving better accuracy in guiding these robotic systems without the need for frequent X-ray scans, patients can experience safer and more efficient medical interventions.

Another critical consideration during robot-assisted surgeries involves regulating the applied force to the target area to avoid accidental perforation or puncture of organs and blood vessels. By maintaining precise control over the force exerted, medical professionals can perform procedures more efficiently and effectively, thereby ensuring enhanced patient safety and optimal surgical outcomes [125]. In conclusion, the development of a universally accessible comprehensive, precise, and fast model that empowers surgical teams to control crucial factors during procedures remains a significant challenge and is highly demanded in the field of medicine. Meeting this pressing need would revolutionize surgical practices, ensuring greater affordability, efficiency, and patient safety. Furthermore, achieving this goal could potentially unlock a wide array of minimally invasive interventional procedures that are currently beyond the reach of existing techniques, thereby empowering robotic systems to revolutionize medical practices and broaden the scope of treatments available to patients [65]. Creating a precise model is a step towards meeting the requirements; however, it falls short of fulfilling the real-time feedback needs due to its complexity and extensive calculations. To accelerate response times and achieve feasible solutions, the incorporation of additional tools becomes necessary, especially through the application of advanced neural network algorithms.

1.1.5 Neural Network

A neural network is a type of artificial intelligence model inspired by the structure and functioning of the human brain (Figure 1.9, right) which is a computational system composed of interconnected nodes (artificial neurons) organized in layers. These nodes work together to process and learn from input data, enabling the network to recognize patterns, make decisions, and perform various tasks [129].

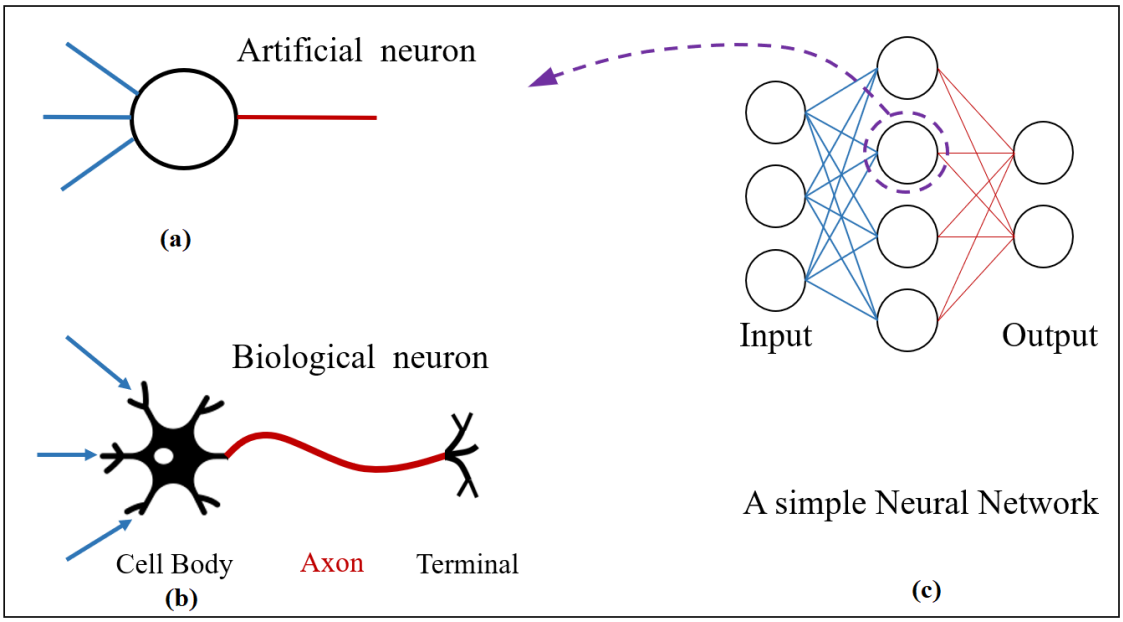

Figure 1.9: A simple artificial neuron (a) and its biological inspiration (b) depicted alongside a schematic of a basic neural network (c)

The basic building block of a neural network is an artificial neuron, also known as a perceptron [28]. Each neuron takes one or more input values, applies weights to them, and then passes the weighted sum through an activation function. The activation function introduces non-linearity to the network, allowing it to learn complex patterns and make non-linear transformations on the input data.

As depicted Figure 1.9, neural networks consist of multiple layers, typically including:

1. **Input Layer:** The initial layer receives raw input data, which could be images, text,

numerical values, or any other type of information.

2. **Hidden Layers:** Intermediate layers between the input and output layers. They process and transform the input data through their interconnected neurons.

3. **Output Layer:** The final layer produces the network's predictions or outputs based on the processed information from the hidden layers.

During the training process, the neural network learns from labeled data by adjusting its internal weights and biases to minimize the difference between predicted outputs and the actual targets. This optimization process is often accomplished using gradient descent and backpropagation algorithms, where the network iteratively updates its parameters to reduce the error between predictions and ground truth.

Neural networks have shown exceptional performance in a wide range of tasks, such as image and speech recognition, natural language processing, machine translation, playing games, medical diagnosis, and more. Their ability to automatically learn features and patterns from data makes them powerful tools for solving complex problems and handling large-scale, high-dimensional datasets. Different types of neural networks have been developed to tackle specific tasks more efficiently. Some popular variations include feedforward neural networks, recurrent neural networks (RNNs), convolutional neural networks (CNNs), and transformer networks, each optimized for different types of data and learning objectives [8].

1.1.6 Neural Network in MIS

Neural networks have demonstrated great potential in diverse applications within the field of minimally invasive surgery. The integration of artificial intelligence (AI) and computer vision technologies into minimally invasive surgery has gained traction. Vision-based detection of surgical instruments has become popular, enabling more precise guidance of surgical robots

and imaging technology [68]. Computer vision-based models, such as object segmentation, detection, and tracking, aid surgeons during surgery and enhance the overall outcomes of minimally invasive procedures [100]. Convolutional neural networks (CNNs) have demonstrated robust performance in instrument recognition and pose estimation [68].

In gynecology, augmented reality (AR) technology has been integrated into the operating room, facilitating predictions of survival after surgery for cervical cancer models, and supporting computer-assisted or robotic platforms to bridge the gap between open and minimally invasive surgical skills [13]. Recurrent neural networks (RNNs) have been employed to estimate forces in robotic tasks, generate force distribution maps, and detect contact transients [40]. Super-resolution techniques have been investigated to enhance perceived resolution in robotic-assisted minimally invasive surgery's foveal field-of-view [72]. Additionally, active vision-based motion compensation schemes have been proposed to address issues related to physiological motion during minimally invasive cardiac surgery [96]. Overall, neural networks have demonstrated promise in diverse applications within minimally invasive surgery, such as reducing adhesions, assisting with instrument detection and tracking, enhancing visual perception, estimating forces, reconstructing the shape, and compensating for physiological motion.

1.1.7 Case study: Ablation procedure

The initial focus of this research revolves around addressing a fundamentally neglected issue in soft robot modeling, much like Hamlet's famous phrase: *to consider or not to consider blood flow effects, that is the question.* To explore this inquiry, a comprehensive case study is conducted, examining catheterization during ablation procedures to assess the impact of blood flow on catheter contact force. As such, it becomes essential to introduce and elucidate the problem at hand before diving into the experimental details in Chapter 2. By doing so,

a clear context is established, laying the groundwork for the subsequent investigation.

Robotic Catheter Ablation is a teleoperated robotic procedure. The robotic system for this procedure has a leader-follower configuration, thus lacking direct human touch on organs and instruments. However, the sense of touch is replaced by force sensor feedback that enables surgeons to monitor the contact force between the catheter and the patient's heart. Due to the high cost of sensorized cardiac catheters, sensor-free force estimation techniques have gained momentum in the state of the art. These techniques, for the most part, neglect the effects of blood flow in the left atrium, while recent clinical evidence suggests that blood flow disturbance can affect the stability and safety of catheter tip-tissue contact. This study was aimed at identifying the mechanisms by which blood flow may compromise tip-tissue contact force and quantifying such effects systematically. To this end, first utilizing a closed-loop flow channel, we examined the effects of blood (represented by water) flow on the magnitude of the tip contact force at physiological and pathological flow rates in 3D-printed pulmonary veins. Also, five configurations of an ablation catheter were considered to investigate the combined effects of catheter deflection and positioning of the catheter tip. Our results show that the tip contact force can greatly change because of the fluid flow, e.g., up to 37% when the catheter is close to the left inferior pulmonary vein. Also, even in the absence of blood flow, the maximum contact force was observed to reduce by increasing the catheter deflection. Diminishing tip contact force was exacerbated at higher flow rates. This study provides a quantitative mechanical explanation of why robotic ablation may result in sub-optimal right inferior pulmonary vein isolation.

Background

Catheter ablation therapy is considered an effective treatment for cardiac atrial fibrillation (AFib). AFib is one the most common types of cardiac arrhythmia in which a sinoatrial

node fails to produce regular electrical impulses. This causes the heart to quiver or fibrillate instead of beating routinely, which as a result, considerably increases the risk of stroke. AFib is linked to several cardiovascular and cerebrovascular issues, and its growing trend among people will pose extra hospitalization costs and extra public health burdens. If the age-and sex-specific prevalence remains stable during the next decades, the prevalence of AFib is estimated to double by 2060 in the European Union [66]. A total of 3.046 million new cases of AFib worldwide were registered in the Global Health Database in 2017, which is a 31% increase since 1997. On current projections, there will be more than a 60% increase in the number of AFib cases by 2050 [76].

AFib intervention is carried out by a surgeon manually or through a robotic-assisted procedure called Robotic Catheter Ablation (RCA). Figure 1.10(a) shows a typical RCA system, and Fig. 1.10.(b) schematically shows a cardiac ablation catheter in contact with atrial tissue. A catheter is essentially a long slender tube, which is inserted into one of the main veins from the shoulder, neck, or groin and is guided to reach the right atrium. Through a small transseptal puncture, the catheter reaches the left atrium (LA). The surgeon then uses the catheter tip to make non-conducting scars (called lesions) on the LA wall using Radiofrequency (RFA) or Cryo-balloon (CRA) ablation technique. The success of RFA is directly linked to the formation of effective lesions, which itself is dependent on the catheter-tissue contact force (CF). Ample clinical evidence suggested a CF between 0.1 to 0.5 N minimizes the risk of AFib recurrence [53]. CFs as high as 0.6 N may cause steam pop and the risk of stroke [81], whereas higher forces may cause LA puncture. On the other hand, CFs below 0.1 N do not make proper lesions to treat AFib. They also put contact stability at risk by reducing the static friction threshold on the catheter tip-tissue contact. This means an increase in the possibility of catheter slippage from the LA wall. Thus, monitoring the CF continuously during ablation is pivotal for the safety and stability of contact.

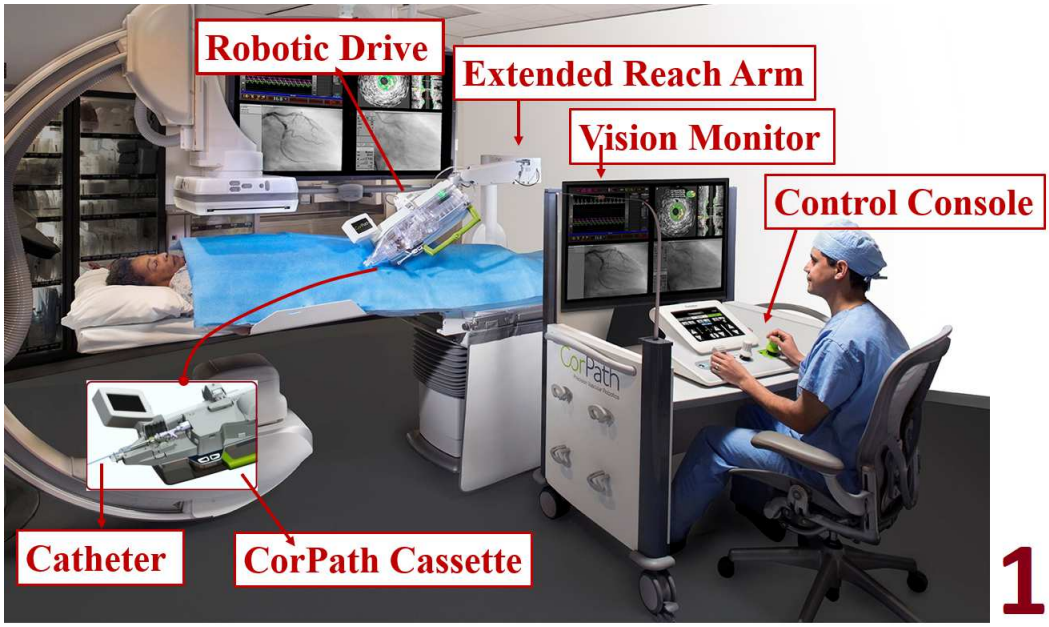

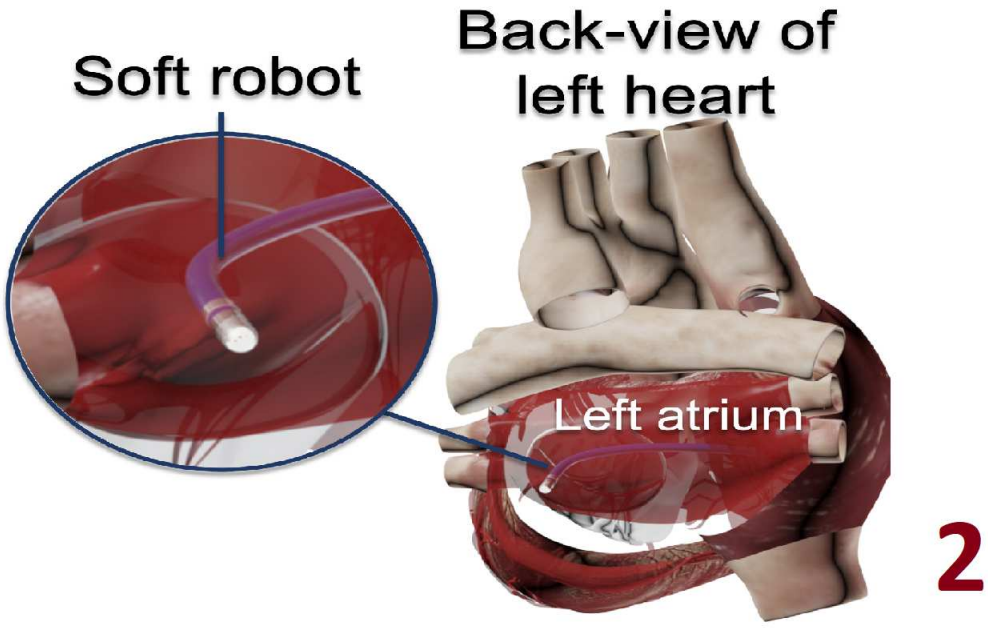

Figure 1.10: (a) A representative robot-assisted cardiac intervention system (CorPathTMGRX robotic PCI system, courtesy of Corindus Inc., Waltham, MA, USA), and (b) cardiac ablation catheter in contact with atrial tissue.

RCA is a more attractive option compared to manual intervention since it reduces the procedure duration and minimizes the operator's fluoroscopy exposure [126]. However, setting up an RCA is a challenging task. In addition, no haptic feedback is provided to the surgeon, and force controlling over the LA wall is indirectly implemented by the robot arm. This is considered as the main limitation of RCA. Thus, catheters with CF sensing technology have been developed. Electromagnetic or fiber optic sensors installed on the tip of catheters continuously give force feedback to help the surgeon to apply sufficient force for ablation. Examples of such technologies are TactiCath™ (Abbot Vascular, CA, US), and Carto® SmartTouch™ (Biosense Webster, CA, US). Although catheters with integrated force sensing technology successfully function in clinical trials, they are not pervasive due to their prohibitive costs, low accuracy of lateral forces sensing [25], and vulnerability to noise due to a chaotic workspace [91]. Moreover, they are not associated with an increased success rate nor a decreased complication rate in ablation [94]. Recently, Torkaman et al. have proposed a low-cost highly flexible force sensor embeddable to the catheter's body [118]; however, similar to other sensor-based solutions, it adds to the complexity of rather simple catheters and hence to the cost [19, 56].

1.2 Literature review

1.2.1 Ablation studies review

Toward developing sensor-free force estimation models, the shape of catheters was used in [17, 55, 58, 62, 101] to estimate the CF. However, virtually all previous sensor-free force estimation techniques neglect the effects of blood flow on the catheter in the LA. Only recently, Hao et al. [53] developed a pseudo-rigid-body model to examine the contact stability and contact safety of a robotic catheter under blood flow disturbances. The blood flow

was assumed to be of uniform velocity, and its effect was modeled via a normal pressure drag. They found that blood flow disturbances can greatly affect the stability and safety of the contact between the robotic catheter and tissue. However, their results are yet to be confirmed by experimental studies.

Since the blood flow in the LA is complex, including vortical structures [45], mathematical models may not be able to fully capture its effects. Thus, experimental studies are in high demand. Franco et al. [43] performed ex-vivo experiments using TactiCath™ and SmartTouch™ catheters in contact with porcine left ventricle portions fixed in a saline bath. They examined the effects of irrigation rate (2-30 ml/min) on the CF before and during ablation. They found that increasing the irrigation rate before ablation led to a slight but significant reduction in CF.

1.2.2 Soft-robot modeling review

In surgical interventions where the trajectory of a flexible robot holds significance, such as angioplasty to track the position of guide wires and catheters [39], endoscopic procedures [26], respirometry stent placement [113], or Transoral surgeries [109], understanding the shape becomes crucial. On the other hand, in certain applications, such as ablation [87] and pathology sampling [123], the magnitude of applied force assumes paramount importance, leading to the emergence of dedicated force estimation methods. In order to acquire information on the shape or force, different methods have been developed in the literature, which are categorized as illustrated in Figure 1.11. The details about these methods are given in the following sections.

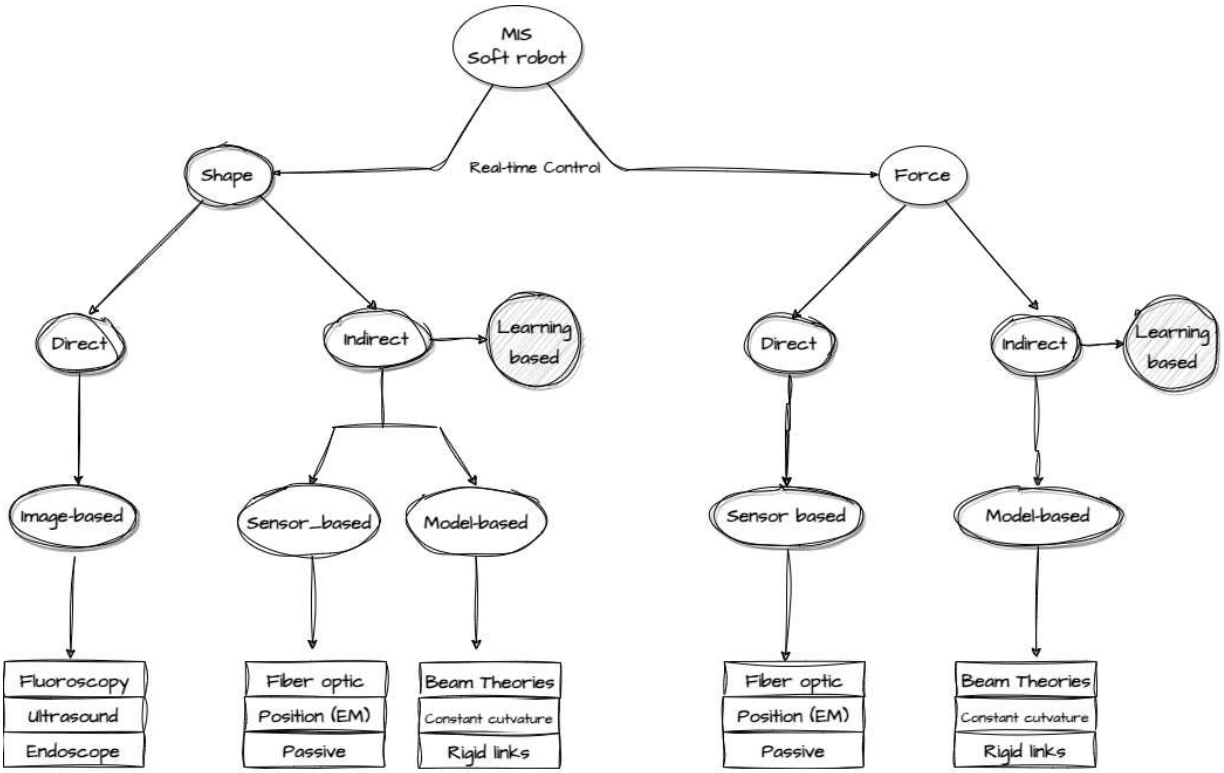

Figure 1.11: Various methods for estimating force or shape of soft robots in minimally invasive surgery applications.

1.2.3 Shape reconstruction

The first branch of methods have been developed to obtain the shape of a soft robot during its insertion into the patient's body. These methods can be classified into two main categories: direct methods and indirect methods. Direct or image-based methods use imaging techniques, such as fluoroscopy, endoscopy, and ultrasound and reconstruct the shape by processing the acquired images. The advantages of these methods include their ability to provide straightforward and direct visualization, as well as real-time measurements. Nonetheless, they have several drawbacks, including high cost, bulkiness, low-speed data acquisition, low signal-to-noise ratio and above all, prolonged patient exposure to radiation [42, 99]. As a consequence of these drawbacks, indirect methods have been developed to reconstruct the shape without the need for direct visualization.

Sensors have widely been utilized to indirectly reconstruct the shape of soft robots. For example, optical sensors were used to reconstruct the shape with a change in the light source [44]. Since they can be made flexible, in miniature size, and immune to electromagnetic interference, they are a good fit for soft robot applications. They can be used to detect curvature, torsion, and control with feedback in real-time [128, 134]. Position sensors (like electromagnetic or inertial measurement units) can measure the relative position and orientation from a fixed or reference point. Real-time tracking, freedom from the line of sight, and accuracy allow tracking the shape of a soft robot during colonoscopy [5]. Guo et al. [50] fitted the variation of a soft robot measured by electromagnetic sensors to a quadratic Bézier curve to reconstruct the shape. Position sensors can also be used in sub-millimeter arteries with impaired flow conditions to use waveform of the actuation signal to optimize the navigation performance [88].

Magnetic sensors possess desirable characteristics such as compactness, affordability, deformability, high sensitivity, and ease of integration into systems; however, the use of permanent magnets creates uneven magnetic fields, posing challenges in their control. These robots require large and complex electromagnetic setups for power and control, limiting their scalability. Additionally, their control is hindered by the presence of nearby metal objects, as the robots are attracted to them [122]. Stretchable sensors are used to reconstruct the soft-robot shape by sensing deformation through capacitance changes. The shape reconstruction process is performed by acquiring the strain or positional information from these sensors. Due to their high stretchability, they are mainly adapted to soft actuators, where the electromagnetic sensors become difficult and time-consuming. The advantages of these sensors include their practicality, acceptable accuracy, consistency in measuring real-time shape in various environments, short response time, small size, biocompatibility, non-toxicity, high sensitivity, and accuracy. However, they are susceptible to noise in turbulent mediums, and their high cost may limit their applicability in certain scenarios [107].

Various attempts have been made to develop mathematical models for soft robots to indirectly obtain the shape. These models are the cornerstone of the model-based methods. The three key models are presented in Figure 1.12. The rigid-links model (see Figure 1.12a) involves representing a soft robot as a series of interconnected rigid links with flexible rotational joints. Roesthuis et al. conducted a reconstruction of the manipulator's shape while advancing through the body using tip force and moment measurements [97]. However, the study did not take into account the influence of fluid inside the body and reported an average maximum error of 1.37 mm. Venkiteswaran et al. utilized the rigid-links model in a quasi-static environment and successfully estimated the deformed configuration with a minimal shape error of 1.2 mm over its length [119]. However, assuming rigid links in the context of continuum structures appears as an oversimplification. Such an assumption can

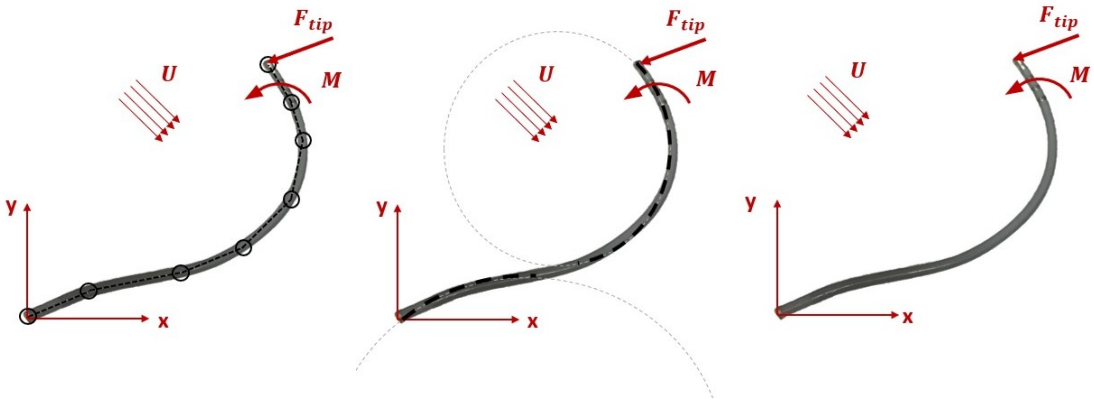

(a) (b) (c)

Figure 1.12: An overview of key mathematical models used for soft robots with a special focus on ablation catheters: a. Rigid-links model, b. Piecewise constant curvature model, and c.Beam model. In the figures, x and y represent the 2-D Cartesian coordinates, F_{tip} and M represent the tip force and moment, respectively; also, U represents the flow velocity.

result in either unrealistic behaviors with few segments or a considerably high number of variables with many segments [119].

Piecewise constant curvature (PCC) refers to a model where a curve or surface is divided into segments with constant curvature. Over each segment, the curvature remains unchanged, but it may change abruptly at the boundaries between segments (see Figure 1.12b). PCC emerges as a powerful model for reconstructing the shape of soft robots. Qi et. al [92] proposed a PCC-based navigation method during catheter insertion in blood vessels. Nonetheless, their approach overlooks the impact of fluid and has significant constraints on miniaturization and on shape trajectory in smaller environments. Most studies, such as Refs. [48, 98] have used single-segment PCC, and only a few (e.g., Ref. [34]) employed a multi-segment PCC in their modeling.

An attractive alternative for modeling soft robots is to use the principles of classical beam theories (Figure 1.12c). Among the numerous studies, the Cosserat rod and Euler-Bernoulli

beam models are the most popular. These models entail solving a set of equilibrium equations that establish the relationship between the position, orientation, force, and moment of the robot. By solving these equations using known values of forces and moments, it is possible to obtain the shape of the robot. Yuan et. al [131] employed the Euler-Bernoulli beam theory to model a surgical robot, considering external forces and moments. Although their solution provided a shape reconstruction model with a 7% error, they did not account for the blood flow forces acting on the robot.

Olson et. al [85] proposed an Euler-Bernoulli beam model to describe the bending behavior of soft robot arms under the combined influence of self-stress and external loads. Ji et. al [60] proposed a simplified design method that involves dividing the actuator into single segments or multiple segments and applying the Euler-Bernoulli beam theory to each segment. This allows for a quick and accurate prediction of the actuator's deflection under different operating conditions. The Cosserat rod model [31] which accounts for the inherent bending, twisting, and stretching behavior of slender rods has emerged as a reliable technique for obtaining the shape of soft robots. Naughton [82] introduced Elastica as a simulation framework that leverages the Cosserat rod model to accurately capture the mechanics of soft robots. Till et. al [117] presented several case studies to demonstrate the application of the Cosserat rod model in real-time simulations, proving the model's ability to capture the intricate deformations and motions of soft and continuum robots. Berthold et. al [22] utilized the Cosserat rod theory to incorporate distributed load and moment, predicting the tip position of a catheter as a soft robot through finite element analysis. They reported a position error of 13%.

With the advent of neural networks and data analysis, learning-based methods have also been developed for estimating the shape of soft robots. The data required for training the neural network (and effectively creating a 'black box') can be collected from real-world

applications or experimental apparatuses or can be synthesized using theoretical models. This black box, given initial force values and characteristics of the soft robot, can be used to reconstruct the shape. Thututhel et. al [114] modeled the soft robot as an Euler-Bernoulli beam and solved it numerically for a range of tip forces to build a data set and trained the neural network using the Bayesian regularization back-propagation algorithm. The fitted network reported 0.0058 ± 0.028 meters position error. One of the key advantages of their work was the modeling of the force and moment of the robot-tissue contact. Next, Thuruthel [115] employed a Cosserat rod model to represent the soft robot and synthesized data for training a neural network. The learning-based framework was used to forecast the real-time trajectory of the robot's tip. In a similar fashion, Pfaff et. al [90] utilized high-dimensional Finite Element Method (FEM) simulation data to train a neural network that can reconstruct and predict the shape of the robot.

1.2.4 Force estimation

As shown in Figure 1.11, there is a second branch of methods aimed at obtaining (or estimating) forces acting on soft robots. Unlike the first branch of methods which focuses on reconstructing the shape, the primary objective here is to determine or predict the force and effectively control it to ensure the success of minimally invasive surgeries. Similarly to the shape reconstruction methods, the force estimation methods are also classified into two main categories, namely direct and indirect methods.

Direct methods, as the name implies, involve directly measuring the forces (and moments) using sensors embedded in the body of soft robots. For example, the most straightforward approach to determine the force acting on a catheter (as a soft robot) during manipulation is by directly integrating a force sensor onto the parts of the catheter that come into contact with the tissue. To date, four different technologies have been commercialized to measure

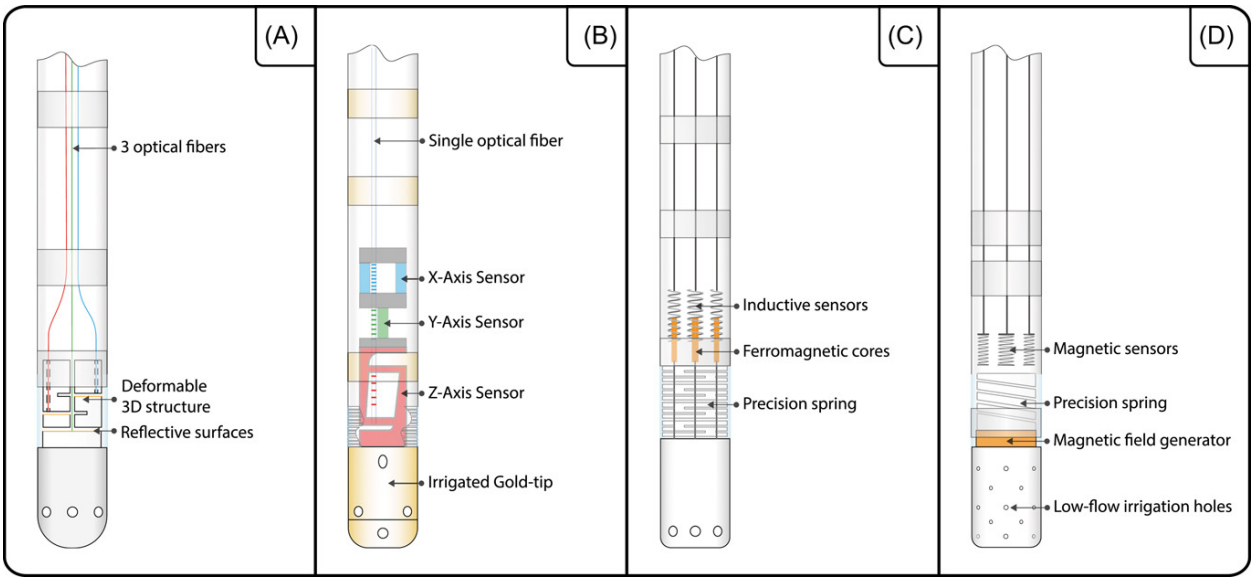

Figure 1.13: Schematic of force sensing technologies: (A) Tacticath™ Quartz (Abbott), (B) AcQBlate® Force (Biotronik), (C) Stablepoint™ (Boston Scientific), (D) Thermocool Smarttouch® SF Catheter (Biosense Webster). Images were adopted from Ref. [67].

contact force at the tip of cardiac catheters [67], as illustrated in Figure 1.13.

Tacticath™ Quartz from Abbott (Chicago, IL, USA) utilizes three optical fibers and Fabry-Pérot interferometers to measure contact force; see Figure 1.13 A. When a force is applied to the catheter tip, the flexible structure changes length, altering the interference pattern and allowing computation of force magnitude and orientation. AcQBlate® Force from Biotronik (Berlin, Germany) employs sensors along multiple axes to measure forces; see Figure 1.13 B. A deformable parallelogram detects axial forces, while separate sensors detect lateral forces. The fiber Bragg grating within an optical fiber reflects different wavelengths based on the force, enabling calculation of the force vector. Stablepoint™ from Boston Scientific (Marlborough, MA, USA) uses a machined precision spring and inductive sensors to measure forces; see Figure 1.13 C. The movement of ferromagnetic cores within the coils of the sensors, caused by deflection of the spring, changes the inductance. Hooke's law and the spring stiffness are used to calculate axial and lateral forces. Thermocool Smarttouch® SF

Catheter from Biosense Webster[1] (Irvine, CA, USA) utilizes a precision spring and magnetic field sensors; see Figure 1.13 D. A magnetic transducer generates a field, causing the catheter tip to move towards the sensors when forces are applied. By analyzing the signal changes in the sensor coils, the force and direction can be determined using Hooke's law and the spring characteristics.

Several studies [9, 25, 67, 78] have evaluated the accuracy of contact force measurements from these force sensors. Despite the great convenience provided by direct force measurement, force sensors often face limitations related to their functionality and construction. The limitations may include non-linear force measurement, force hysteresis (delayed response to force changes), bulkiness, coupling effects between longitudinal and lateral forces, inaccurate force estimation, and the complexity of design, assembly, and very importantly, their high costs.

These limitations have motivated researchers to explore indirect methods for estimating forces acting on soft robots. In this regard, model-based methods for force estimation, which involve with solving mathematical equations inversely, are considered very promising. More precisely, mathematical models, such as rigid-links, piece-wise constant curvature, and beam models (including Cosserat rod and Euler-Bernoulli beam models), typically used for shape reconstruction, are treated differently, where the shape is known (e.g., through imaging techniques) while forces are unknown. Hence, these model-based methods are sometimes referred to as 'inverse solutions' or 'inverse modeling' techniques.

Hooshiar et. al [57] developed and validated a force estimation framework based on Bézier spline shape approximation and inverse Cosserat rod model. They obtained the necessary condition for the Bézier spline approximation of a constant bending radius catheter. Using the proposed technique, the kinematics and balance equations were solved to calculate the

[1]The company is part of the Johnson&Johnson family of companies.

tip force. Experimental results showed good agreement between the estimated and reference forces, with a mean absolute error of 0.024 ± 0.020 N. Nevertheless, the study oversimplified the soft robot configuration by considering it as a section of a circle with a force and a moment applied at the tip. Adagolodjo et. al [7] devised an inverse modeling technique for soft robots using the Cosserat rod model and developed a coupled numerical method for solving the equations. Despite demonstrating enhanced efficiency, the method was computationally expensive. Additionally, a further simplification was made by solely considering a force and moment at the tip, rendering it unsuitable for soft robots which are in contact with fluid flow.

Using the rigid-links method, Back et. al [15, 16] developed a model for soft robots and employed numerical techniques to estimate the forces involved, the results of which were then validated against experiments. Although their proposed method was intended for the use in the ablation procedure, the order of magnitude of forces considered in the studies exceeded the typical range encountered in the procedure. They considered forces up to 2 N in [15] while in practice the tip force does not exceed 0.5 N. In addition, in both modeling and experiment, the working fluid was assumed to be air, ignoring the effects of blood flow.

Few studies have examined the effects of a surrounding stationary or flowing fluid on the shape or forces acting on soft robots. Gong et. al [47] designed and tested a soft robotic arm for underwater manipulation. In addition to field tests, some tests were performed in a water tank (with still water) to examine the flow pattern and to measure how much force and moments are generated as the soft manipulator was moving underwater. They also utilized the inverse kinematics approach to determine the required joint angles and positions of the soft robotic arm, taking into account the desired end-effector position. Nevertheless, the effects of fluid were not included in the modeling. Hao et. al [51–53] employed a pseudo-rigid-body model to represent the catheter as a soft robot, taking into account the effects of

a uniform blood flow applied perpendicular to the catheter. Khoshbakht et. al [64] designed a flow circuit, and for the first time, experimentally evaluated the effects of fluid flow on the ablation catheters. They reported a 10%-70% change in the tip force components as a result of fluid flow.

The accuracy and efficacy of model-based methods for force estimation heavily depend on how holistic their underlying mathematical models are as well as on the computational complexity. To address the challenges faced by model-based methods, learning-based methods have recently emerged. To employ these methods effectively, a sufficiently large data set is required for training the neural network to accurately predict force based on known shapes. Sayadi et. al [102] introduced and validated a novel learning-based framework for estimating forces in steerable catheters. The framework employed the learning-from-simulation principle and utilized a Bézier shape-fitting method to reduce input space dimensions. Nonlinear regression models, such as Artificial Neural Networks (ANN), and Support Vector Regression (SVR) were used and demonstrated acceptable accuracy within the clinical requirements range.

The present study bridges a significant research gap by considering the effects of fluid flow on the shape reconstruction and force estimation of soft robots. First, a model-based method is developed for shape reconstruction. More precisely, the Euler-Bernoulli beam theory is used, which relates the known tip force, tip moment, and fluid flow properties, to the curvature of the soft robot. Instead of solving the differential equation analytically or computationally, the shape is approximated by a Bézier curve, and a minimization problem is formulated to find the Bézier curve control points. The results from this model are compared with those from FEM simulations. One limitation of the proposed model-based method is its relatively long run-time. To address this issue, next, the numerical results from the model are utilized to build a dataset which is then used to train, validate and test a learning-based

model. It will be shown that this model is accurate and about 50 times faster than the model-based method. Since in some applications, such as sensorless ablation catheters, tip force estimation is crucial, a second learning-based model is developed, in which the tip force is assumed to be unknown while all other variables are considered as known. Again, the data obtained from the model-based method is leveraged for training, validation, and testing. The force estimation results from this learning-based model are compared with experimental results, where a fair agreement between the two sets is observed.

1.3 Problem Definition

As discussed in section 1.1.4, there is a significant clinical demand for the development of a comprehensive soft robot model during surgery, allowing the surgical team to have precise control over the robot's movements inside the body and regulate the applied force accurately to the surgical target. This model has the potential to enhance surgical precision and reduce the reliance on advanced imaging equipment and highly-cost force-sensing techniques commonly used in robotic-assisted surgery.

As highlighted in section 1.2, various attempts have been made to create such models, each based on different principles, each with its own set of advantages and disadvantages. However, achieving a more comprehensive and accurate model requires minimizing simplifications and ensuring that the model conditions closely resemble real surgery conditions. By refining the soft robot model and reducing simplifications, surgeons can gain better insights into the robot's behavior during the procedure. This would enable them to control the robot more effectively, leading to improved surgical outcomes. Additionally, with a more robust model, the surgery team can better understand how the applied forces interact with tissues,

enhancing safety and reducing the risk of potential complications. The significance of developing a comprehensive model lies in its potential to decrease the dependence on high-tech imaging and force-sensing technologies, making robotic surgery more accessible and cost-effective. Moreover, with precise control over the soft robot's movements and applied forces, surgeons can conduct surgeries with greater accuracy and confidence, particularly in delicate and complex procedures.

In conclusion, the quest for a comprehensive soft robot model in surgery is driven by the need for precise control, enhanced surgical precision, and reduced reliance on advanced equipment. By minimizing simplifications and closely aligning the model conditions with real surgery scenarios, researchers aim to create a powerful tool that can revolutionize robotic surgery and improve patient outcomes.

1.4 Research Objectives

The primary objective of this study is to develop advanced models for accurate real time shape reconstruction and tip-force estimation of ablation catheters in contact with fluid flow. The following sub-objective work toward achieving the primary objective:

1. to examine the hypothesis that the fluid flow may have significant effects on the tip-force and shape of catheters, some experiments were performed in a one-of-a-kind experimental apparatus.

2. To develop a mechanistic model for accurate shape reconstruction of a soft robot subjected to a tip-force, a tip-moment and a distributed load due to fluid flow. This model will then be used to create a data set which will be used for developing artificial intelligence neural network (NN) models.

3. To develop NN models for real time shape reconstruction and tip force estimation of soft robot in contact with fluid flow. The former enables real time shape reconstruction of soft robot without the need for imaging equipment. The latter enables continuous monitoring of the tip-force of the soft robot without the need for force sensors.

1.5 Contributions

The subsequent list outlines the publications and also the author's and co-authors' contributions made during the course of this master's research:

1. Reza Khoshbakht, Mojtaba Kheiri, Javad Dargahi, and Amir Hooshiar, "Effects of Blood Flow on the Tip Contact Force of Cardiac Ablation Catheters," *2022 IEEE International Symposium on Robotic and Sensors Environments (ROSE), Abu Dhabi, United Arab Emirates, 2022, pp. 1-7.*

   The first author designed and assembled the experimental apparatus, designed and performed experiments, analysed the experimental results and drafted. The second author provided valuable assistance in the preparation of the experimental setup, and interpretation of results, and contributed to the review and editing process of the paper. The third author provided funding and offered guidance and support throughout the research. Additionally, the fourth author actively participated in the construction of the experimental setup and provided inputs during the review and editing stages of the paper.

2. Reza Khoshbakht, Mojtaba Kheiri, Javad Dargahi, and Amir Hooshiar, "Physics-informed Neural Network Modeling of Quasi-static Soft Robots for Percutaneous Interventions,". Submitted to: *International Journal of Solids and Structures.*

The first author performed research about various shape reconstruction and force estimation methods, led the conceptualization and development of the mechanistic and NN models, performed analysis and drafted the paper. The second author contributes to the conceptualization of the mechanistic model, interpretation of the results and reviwing and editing the paper. The third author provide feedback on the model and numerical results. The fourth author contributed to the conceptualization of the neural network reviewing and editing the paper.

1.6 Thesis Layout

This thesis follows the manuscript-based style in accordance with the "Thesis Preparation and Thesis Examination Regulations for Manuscript-based Thesis" of Concordia University's School of Graduate Studies. It is composed of the following chapters:

Chapter 1 presents the identified clinical need and the limitations observed in previous attempts have served as the driving force behind the motivation to develop a model and shape the direction of this research

Chapter 2: Presents the development of a one-of-a-kind experimental apparatus to examine the effect of fluid flow on the tip-force of ablations catheters. The results from five cases are presented and discussed. The experimental results from one of the cases are also used in chapter 3 to validate a neural network model developed for tip-force estimation of soft robot.

Chapter 3: A mechanistic model was proposed to reconstruct the shape of a soft robot based on the applied forces while considering the fluid effect as a distributed load. The model utilized Bezier curves to fit the highly nonlinear equations derived from the problem and solved them using a minimization solution. The accuracy of the proposed solution was

validated by comparing it with Finite Element Method (FEM) results obtained from Abaqus software under the same loading conditions. The results met the accuracy requirements, but due to high numerical calculations, real-time responses were not feasible. To address the speed issue, a neural network solution was implemented. A dataset was generated by running the model for a valid range of forces, and the Bayesian algorithm was selected to train, validate, and test the neural network and the results were presented and discused.

In the second part of this chapter, the reverse route was explored to demonstrate that the proposed model could also predict forces based on shapes during surgeries where force monitoring is critical. Another neural network was trained using shape data as input to estimate the force. The results of this neural network were compared with the results of one of the cases of the experiments conducted in the previous chapter. and the results were presented and discused.

Chapter 4: presents the conclusions drawn from the current study and proposes potential extensions for future research based on the findings. These proposed extensions can serve as a reference for further investigations building upon the present work.

Chapter 2

Effects of Blood Flow on the Tip Contact Force of Cardiac Ablation Catheters

2.0.1 Objectives and Contributions

In this study, to continue our previous works on the fluid-structure interactions of flexible slender structures (modeling, e.g., an ablation catheter in the LA) [111], we have experimentally investigated the hemodynamics (drag) and deflection effects (force transmissibility) on the catheter-tissue contact force. The main contribution of this study is in providing experimental evidence on hypothesized mechanisms of CF variation in human LA at different anatomical locations. In the following, we have described the methodology in Sec. II, including the experimental set-up, procedure, and test cases, and discussed the key results and findings in Sec. III. Concluding remarks are also presented at the end.

2.1 Methodology

To investigate the effects of blood flow on the catheter and, in particular, on the contact force, an in-vitro ablation procedure is designed based on the anatomical characteristics of AFib patients in terms of blood flow rates and pulmonary veins dimensions and directions. The three-dimensional contact force is measured in the presence of water flow at various flow rates. The numerical values are then compared with the contact force measured in air.

2.1.1 Experimental setup

Fig. 2.1 shows the components of a closed-loop experimental set-up built to simulate blood circulation during the ablation procedure. For simplicity, the fluid flow was kept steady. Nevertheless, the anatomy of pulmonary veins allowed for dynamic vortices formation.

To simulate an ablation procedure, an 8Fr Ablation Catheter (Blazer II XP, Boston Scientific, MA, USA) was used. Also, four Digiten G3/8 Hall effect flow sensors were used for continuous flowmetry. The flow sensors were calibrated against a standard flow meter (Cole Parmer, IL, USA). The flowmeters were interrogated by an Arduino Mega 2560 with custom-developed firmware developed in C++ programming language. In addition, a six-axis Force / Torque sensor (Mini40, ATI Industrial Automation, NC, USA) was used for catheter tip force measurements. Water was used as the working fluid, which is circulated with two Deluxe 1056 GPH submersible pumps. The setup was installed on 3D-printed housings. As shown in Fig. 2.1(a), water was pumped from a reservoir and was split into 4 outlets, each connected to a pulmonary vein. The flow in these branches was adjusted manually using four needle valves. The setup was capable of supplying flow rates up to 350 LPH (liters per hour) [70].

As seen from Fig. 2.1(b), two parts were designed based on real dimensions and angles

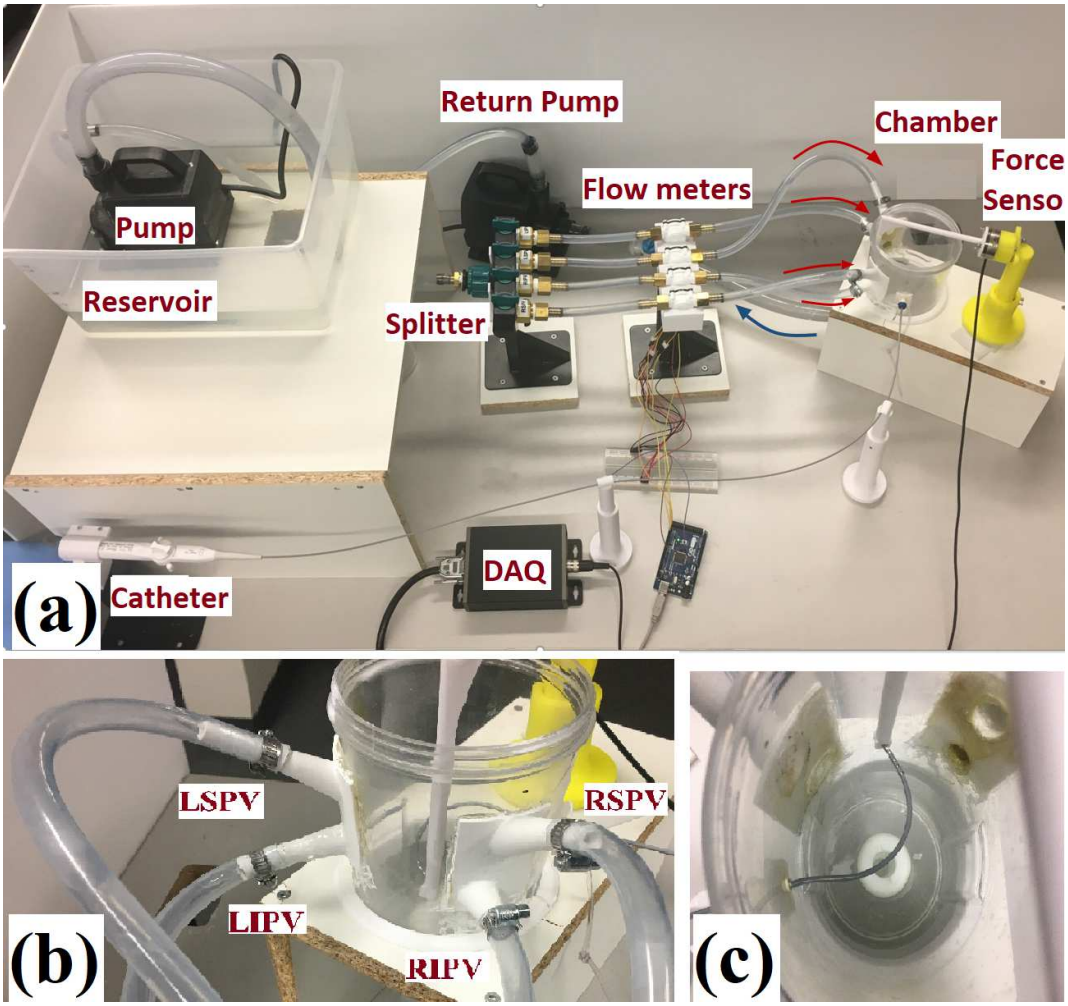

Figure 2.1: (a) Experimental setup components. The red arrows show the flow path from the reservoir towards the chamber. The blue arrow shows the flow direction from the chamber towards the reservoir, and (b) the LA phantom with four 3D-printed pulmonary vein inlets. L/R: left/right, I/S: inferior/superior, PV: pulmonary vein, and (c) shows the fixed contact point.

of pulmonary veins when they reach the left atrium [21]. They were 3D-printed and glued externally to the chamber. These parts ensure that the fluid enters the chamber with proper velocities and at proper angles. The chamber (or the test section) was cylindrical in shape, was rigid, and was made of transparent plastic. The chamber was larger in volume compared to an actual left atrium, which allowed easy access and a better view. The fluid inside the chamber was drained through a hole made to the bottom of the chamber. The size of the drain hole is equal to that of the mitral orifice of the LA according to the anatomical references [86]. A small orifice was made in the wall of the chamber opposite the PVs (which mimicked a transseptal puncture) to let the catheter in the chamber. The hole was sealed with an 8-Fr introducing sheath.

Since the force sensor used in these experiments was not water-resistant, an indirect force measurement method was adopted. An L-shaped rod was designed and 3D-printed to transmit the force from inside the chamber to the outside. The rod, i.e. force transmitter, was secured on the force sensor at one end. A tiny dimple was made to the free end of the force transmitter which was placed close to (but not touching) the interior of the lateral surface of the chamber. As a result, small moments are also generated at the contact point. The horizontal, vertical, and angular positions of the contact points inside the chamber were selected based on the common clinical ablation sites [93].

2.1.2 Tests Protocol

Various experiments were conducted to measure the contact force in the presence of fluid flow. In all the experiments, the following procedure was followed to collect data:

1. The force transmitter tip is placed at the desired location (or ablation site) inside the empty chamber.

2. The force sensor is started at zero.

3. The catheter is inserted into the chamber and is made in contact with the force transmitter. The catheter is deflected using its shape deflector knob to reach the desired reference (or nominal) CF denoted by $F_{c,ref}$.

4. The force sensor is set at zero, again.

5. The pump is started, and the flow rate is slowly increased to the desired value by adjusting the splitter valves. Enough time is permitted for flow to reach a steady state. Then, force measurement is performed at the sample rate of 62.5 Hz over 250 Seconds. This force is denoted by F_{tot}.

6. The pump is turned off; the chamber is drained, and the catheter is removed from the chamber.

7. The force sensor is set at zero.

8. The pump is started, and the flow rate is slowly increased to the value(s) in step 5. After the flow reaches the steady state, force measurement is performed. This is the force due to fluid flow, acting on the force transmitter. This force is denoted by F_{trans}.

The fluid force is obtained from $F_{c,f} = F_{tot} - F_{trans}$. To obtain the contact force which also includes the fluid effect, one should add the contact force in air, $F_{c,ref}$, to $F_{c,f}$, i.e., $F_f = F_{c,f} + F_{c,ref}$. Figure 2.2 shows different contact arrangements between the catheter and the free end of the transmitter at contact point C.

2.1.3 Test Cases

Five sets of experiments were conducted, the summary of which is given in Table 2.1. One of the most frequent targets for the ablation procedure is on the LA wall around pulmonary

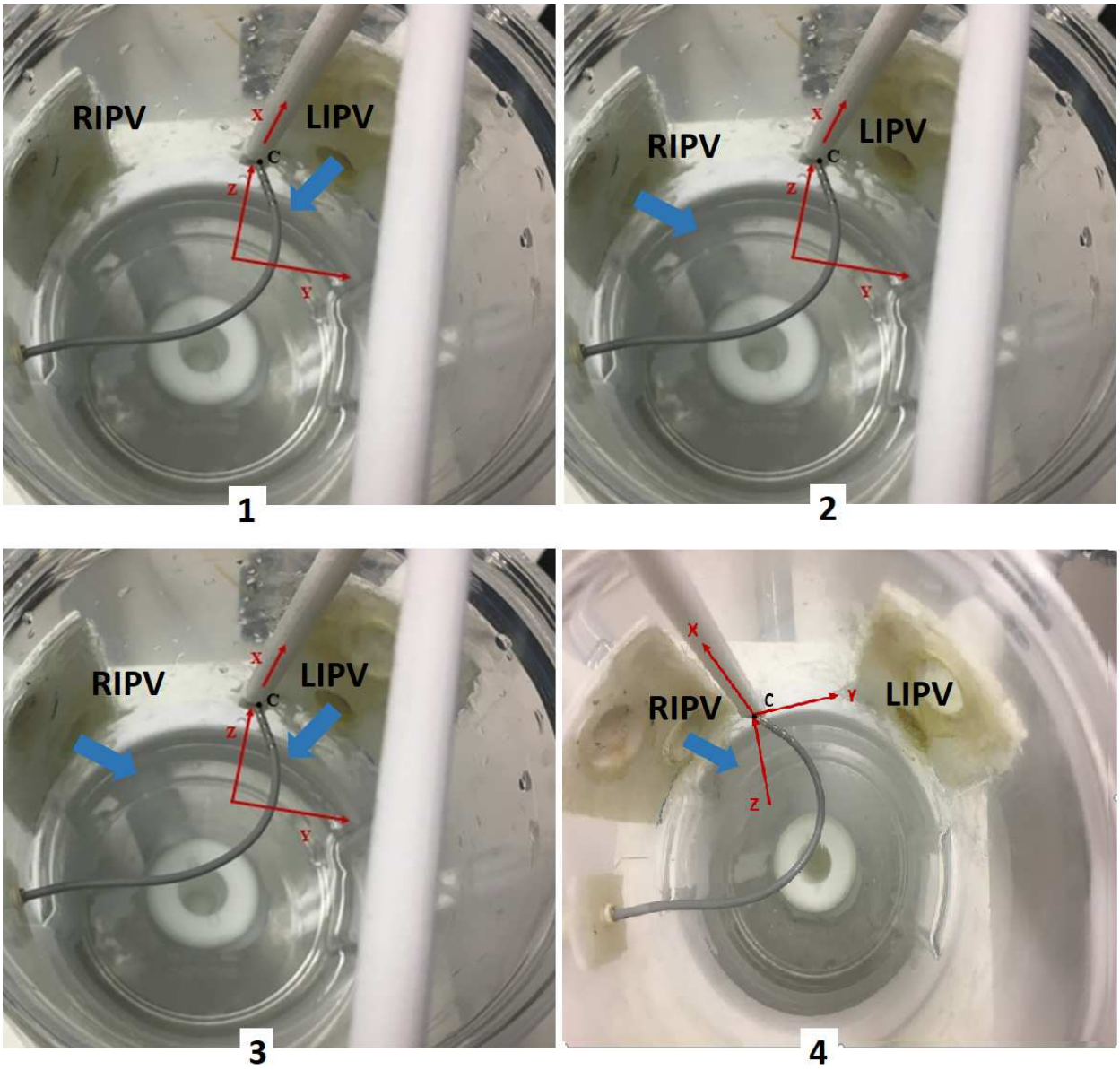

Figure 2.2: Different arrangements considered in the present experiments: (a) the ablation site is in the vicinity of the LIPV outlet, and flow enters the chamber from the LIPV, (b) the ablation site is in the vicinity of the LIPV outlet, and flow enters from the RIPV, (c) the ablation site is in the vicinity of the LIPV outlet, and flow enters from both LIPV and RIPV, and (d) the ablation site is in the vicinity of RIPV, and flow enters from the RIPV. The blue arrow shows the flow direction into the chamber. The red arrows represent the coordinate system attached to the force sensor. Also, the contact point is marked by C.

veins outlets [93]. In the table, an ablation site refers to the position of the force transmitter tip. For example, if the tip is placed in the vicinity of the outlet of the LIPV, then the ablation site is called LIPV. Figure 2.2 shows the different arrangements considered in the present experiments.

Table 2.1: Conditions and initial forces in the present experiments

				Reference CF (N)		
Case	Site	LIPV	RIPV	Fx	Fy	Fz
1	LIPV	Open	Closed	-0.078	0.1029	0.284
2	LIPV	Closed	Opened	-0.048	0.085	0.246
3	LIPV	Open	Open	-0.078	0.089	0.265
4	RIPV	Closed	Open	-0.037	-0.058	0.2023
5	RIPV	Closed	Open	-0.025	-0.018	0.1044

2.2 Resutls and Discussions

Here, some results on the variation of the three-dimensional (3-D) tip CF as a function of the flow rate into the chamber are presented. These results show if the CF in the presence of fluid flow is higher or lower and by how much, compared to the reference CF (i.e., the CF in the air). The results are summarized in Figs. 4 - 8 and Tables 2 - 6. The figures show the variation of the mean value of the CF (in N) in the x-, y-, and z-directions, represented by F_x, F_y and F_z, respectively. In all the figures, the lighter color represents the reference CF, the darker color shows an increase, and the hatched pattern represents a decrease in the CF caused by fluid flow. The tables, on the other hand, report the relative change (in percent) in the CF and the standard deviation of measurements (in N). The selection of the coordinate system is not arbitrary; it is based on the coordinate system associated with the force sensor. Considering the orientation of the catheter in test cases 1 - 5 (see Fig. 2.2), one may conclude that F_z for the most part works as the normal component of the contact force

while F_x and F_y may be considered as the tangential components. The tangential forces are due to surface friction and reaction forces by the walls of the tiny dimple on the force transmitter end. The magnitude of the normal contact force is crucial for both the safety and stability of the ablation procedure while the tangential components are the key for the stability of the catheter.

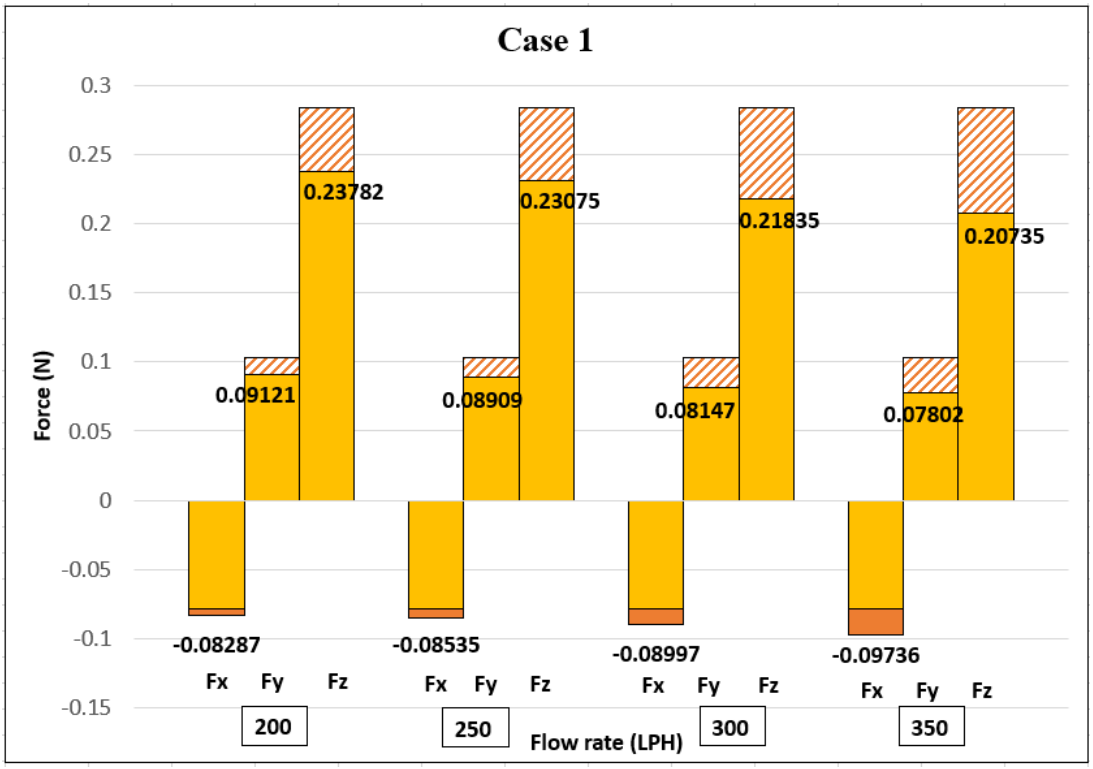

Figure 2.3: The variation of the mean value of the 3-D CF as a function of the flow rate for case 1.

See Fig. 2.3 which shows the results for test case 1; refer also to Table 2.1 and Fig. 2.2(a).

Table 2.2: Effect of flow rate on the CF in case 1.

Flow Rate (LPH)	F_x Impact %	St.Dev	F_y Impact %	St.Dev	F_z Impact %	St.Dev
200	6.036	0.00412	011.36	0.00412	-0.16289	0.00422
250	9.211	0.00772	-13.421	0.00580	-18.776	0.00451
300	15.122	0.01075	-20.821	0.00783	-23.142	0.00605
350	19.974	0.01195	-24.181	0.00896	-27.014	0.00739

As seen from the chart, for all three components, by increasing the flow rate, the difference between the force under the fluid flow and the reference force becomes larger. This is very much expected as the force applied by the fluid flow is theoretically proportional to the flow velocity (and thus flow rate) squared. It is also seen that because of the fluid flow, the magnitude of F_x increases (with respect to the reference value) while F_y and F_z decrease. Both the reduction of F_z and the increase in F_x have adverse effects on the stability of the catheter. Considering the so-called stability cone [112], both these would increase the possibility of slippage. In contrast, the reduction of F_y is favorable for the stability and may compensate for the destabilizing effects of the other two components. The increase in F_x and the reduction in F_y and F_z under the fluid flow may be explained as follows. As shown in Fig. 2.2 (a), the fluid inside the chamber leaves the chamber through a hole at the bottom, which in fact causes a secondary flow and thus a force in the downward direction (i.e., -x-direction). This force becomes stronger by increasing the flow rate, as evidenced by the values given on the chart. On the other hand, the direction of the flow entering the chamber through the LIPV is such that it pushes the catheter in the -y and -z-directions, which as a result, reduces the contact forces in those directions with respect to the reference values.

Table 2.3: Effect of flow rate on the CF in case 2

Flow Rate (LPH)	F_x Impact %	St.Dev	F_y Impact %	St.Dev	F_z Impact %	St.Dev
200	5.377	0.00192	5.5172	0.00261	-4.80474	0.00231
250	8.9901	0.00191	9.0085	0.00319	-7.16587	0.00286
300	16.3954	0.00288	11.5299	0.00338	-16.15509	0.00454
350	20.1050	0.00338	12.2064	0.00364	-24.71779	0.00475

From Table 2.3, one can conclude that the fluid flow impacts F_z the most, where the maximum change is approximately 27%. This occurred at the flow rate of 350 LPH. The relative changes in F_x and F_z are also comparable, with the maximum of approximately

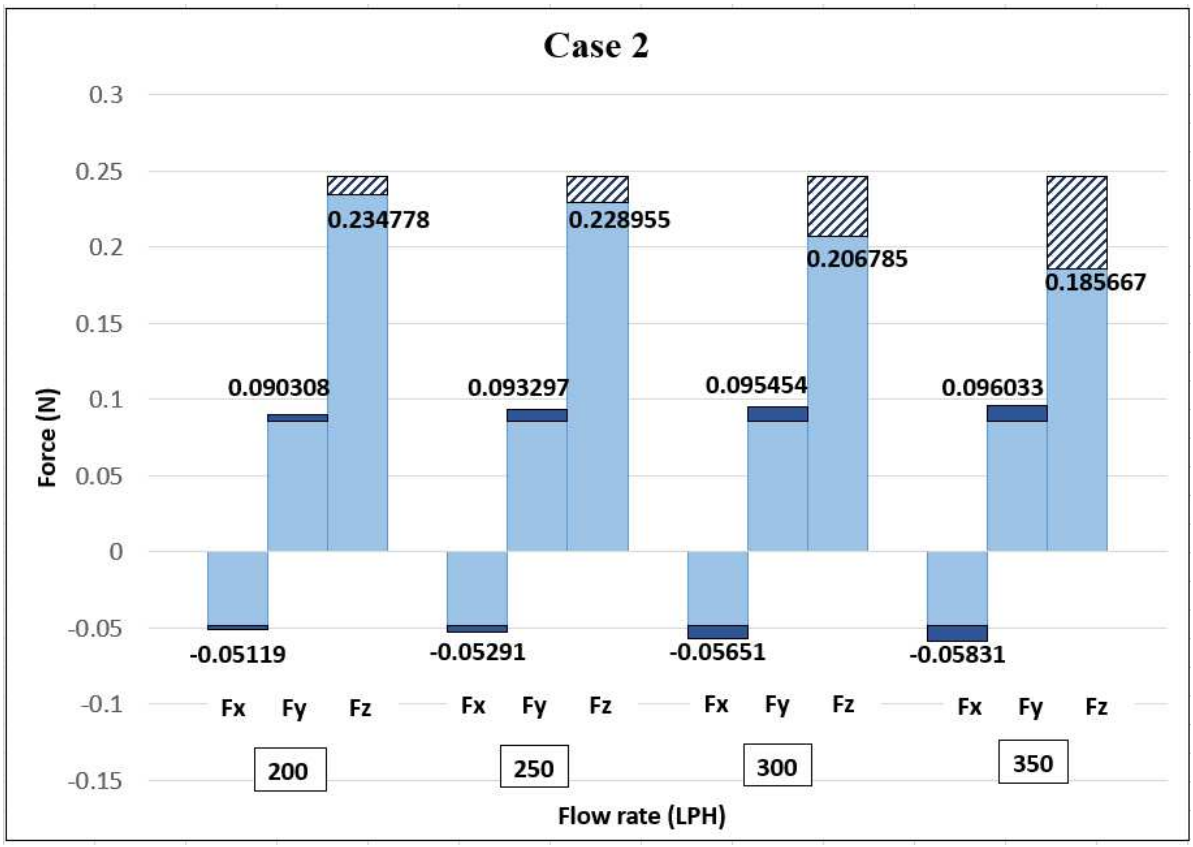

Figure 2.4: The variation of the mean value of the 3-D CF as a function of the flow rate for case 2.

20% and 24%, respectively. As also seen in Table 2.2, the standard deviation for all force components increases with the flow. Stronger vortical structures are expected to develop inside the chamber at higher flow rates. These would create stronger flow disturbances and thus more fluctuations in the fluid forces. The standard deviation is particularly higher for F_x, where it can be as large as 10% of the mean value.

Fig. 2.4 shows the results for test case 2 where the flow enters the chamber via the RIPV. Interestingly, very similar observations as those for case 1, can be made here. The only exception is that, in case 2, F_y increases above the reference value due to fluid flow. This can be understood by examining the direction of the flow into the chamber from Fig. 2.2(b). As seen, the flow entering the chamber through the RIPV pushes the catheter in

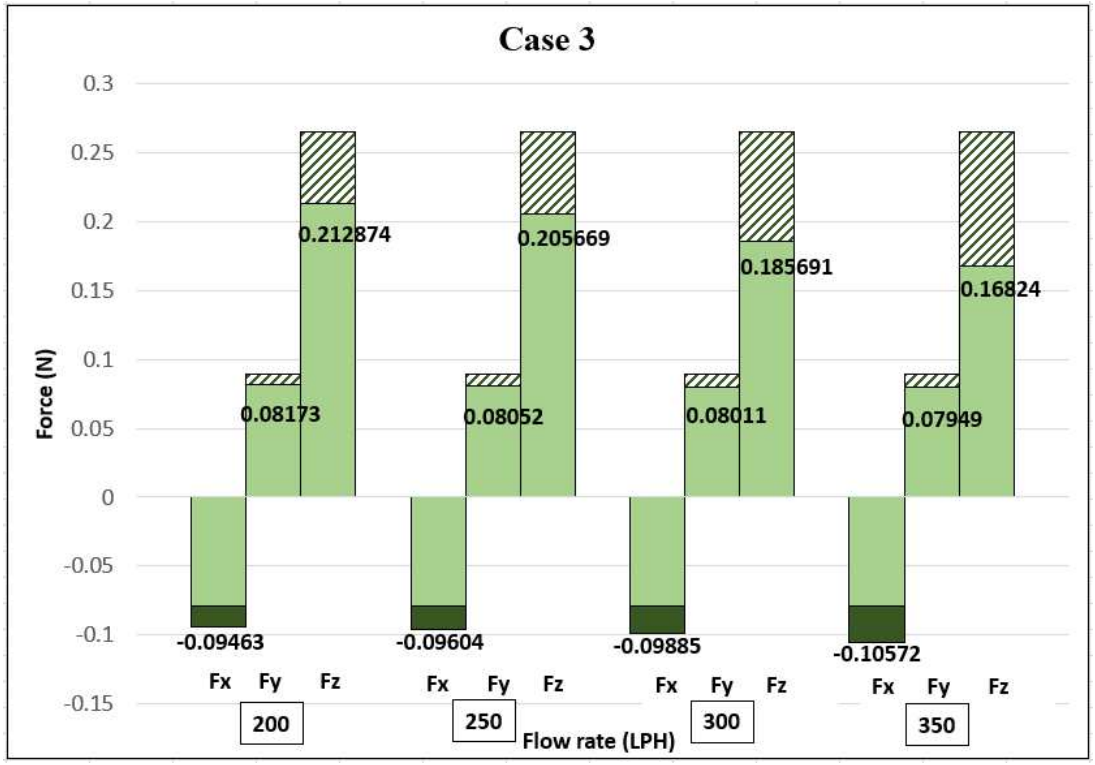

Figure 2.5: The variation of the mean value of the 3-D CF as a function of the flow rate for case 3. The flow rates given in the chart are only for one of the veins. The actual flow rates are two times of those given above.

the y-direction. Comparing cases 1 and 2, case 2 appears to be more critical from the stability point of view. This is because the reduction in F_z and the increase in F_x and F_y, all are unfavorable changes. As seen from Table 2.3, the impact of fluid flow on F_y has been significantly reduced, when compared to case 1. For F_x and F_z, the impact is almost of the same magnitude with the maximum of 20% and 24%, respectively. Force fluctuations appear to be significantly less in case 2, as evidenced by very small standard deviations.

Figure 2.5 shows the results for case 3. As seen from Figure 2.2(c), in case 3, both the LIPV and RIPV are open and the total flow rate into the chamber is almost double the flow rate in case 1 or 2. Thus, case 3 results may be considered as an aggregation of those from cases 1 and 2. From what discussed above, one can conclude that F_x due to the LIPV flow

and that due to the RIPV flow add up, which introduces a larger change to the reference F_x. A similar cumulative effect can be seen for F_z. In contrast, for F_y, the two flows weaken each other. Since the LIPV flow shows a stronger impact, the overall behavior of F_y is similar to that in Figure 2.3. Compare the heights of hatched and dark-color regions on the bars in Figure 2.5 with those in Figure 2.3 and 2.4. The numbers given in Table 2.4 confirm the cumulative effect of the LIPV and RIPV flows on F_x and F_z and their competing role in F_y. The maximum change in F_z is approximately 36% while it is 34% and 11% for F_x and F_y, respectively.

During a PV circumferential ablation, reaching regions around the RIPV is typically hard. This is due to the location of the RIPV with respect to the transseptal puncture. As a result, the catheter needs to be considerably bent (as also shown in Figure 2.2(d)) which limits the force that can be applied by the surgeon. For these reasons, cases 4 and 5 have been designed to examine the effects of fluid flow on the CF when the catheter is in the vicinity of the RIPV.

Figure 2.6 shows the results for case 4. The maximum force in the z-direction, achieved in air by pushing and bending the catheter was approximately 0.2 N. As seen from the bar chart, the most significant change due to fluid flow occurs to F_z. This is also confirmed from Table 2.5, where the maximum change in F_z is around 30%, which occurs at 350 LPH. The maximum changes in F_x and F_y are about 16% and 25%, respectively. The fluid flow reduces the magnitude of the reference F_z and F_y while similarly to cases 1 to 3, increasing the

Table 2.4: Effect of flow rate on the CF in case 3.

Flow Rate (LPH)	F_x Impact %	St.Dev	F_y Impact %	St.Dev	F_z Impact %	St.Dev
200	20.371	0.00311	8.7983	0.00264	-19.7841	0.00436
250	22.164	0.00376	10.1494	0.00327	-22.4991	0.00483
300	25.737	0.00422	10.6054	0.00385	-30.0227	0.00496
350	34.47423	0.00505	11.2895	0.00451	-36.6031	0.00585

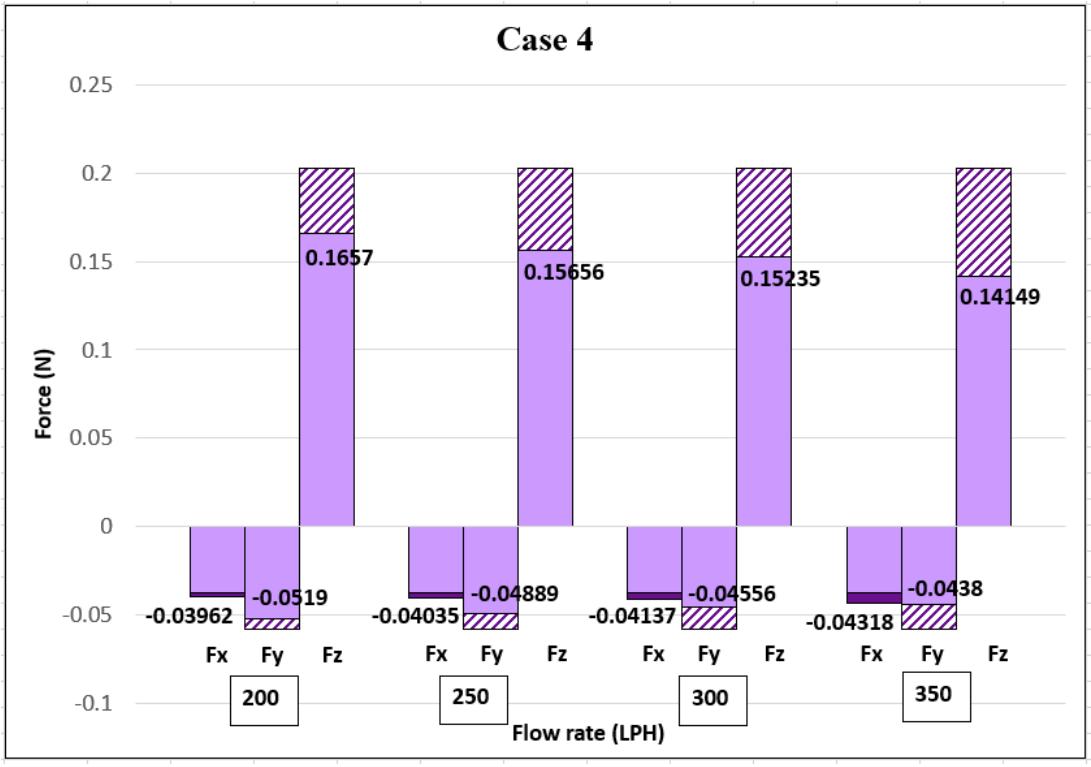

Figure 2.6: The variation of the mean value of the 3-D CF as a function of the flow rate for case 4.

magnitude of the reference F_x. Again, these can be explained by considering the orientation of the coordinate system, the catheter, and the incoming fluid flow.

Case 5 is the same as case 4 with the exception that the reference contact force is set close to 0.1 N which is the minimum limit for a successful ablation [**?**]. As seen from the bar chart shown in Figure 2.7 and confirmed by the numerical values given in Table 2.6, the impact of the fluid flow becomes more pronounced in this case. For example, F_z reaches a maximum reduction of 47%, and the maximum reduction in F_y becomes approximately 70%. These large changes are not because the fluid flow forces are stronger in case 5. They are because the magnitude of the reference CF is now comparable to the magnitude of the fluid forces. As seen from Figure 2.7, at any of the flow rates, F_z ¡ 0.1 N. Assuming that the normal contact force is mainly due to F_z, this means that the ablation would inevitably

Table 2.5: Effect of flow rate on the CF in case 4.

Flow Rate (LPH)	F_x Impact %	St.Dev	F_y Impact %	St.Dev	F_z Impact %	St.Dev
200	6.515	0.00574	10.847	0.00393	18.103	0.00477
250	8.489	0.00690	16.014	0.00561	22.618	0.00534
300	11.216	0.00882	21.742	0.00701	24.253	0.00696
350	16.099	0.01004	24.767	0.00865	30.069	0.00983

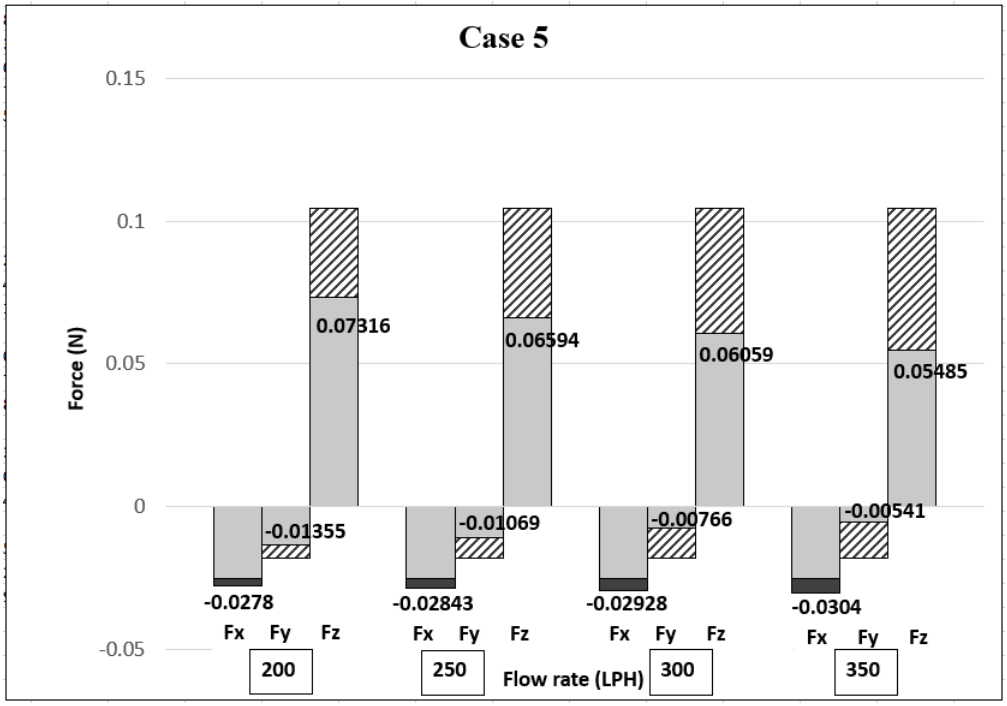

Figure 2.7: The variation of the mean value of the 3-D contact force as a function of the flow rate for case 5.

fail. On the other hand, with a significantly small normal contact force, the contact stability would also be in jeopardy.

2.3 Conclusion

We have built an experimental apparatus in which water with realistic flow rates and angles entered the chamber and flowed over an RFA catheter. By subjecting the catheter to various

Table 2.6: Effect of flow rate on the CF in case 5.

Flow Rate (LPH)	F_x Impact %	St.Dev	F_y Impact %	St.Dev	F_z Impact %	St.Dev
200	8.343	0.00308	25.264	0.00286	29.981	0.00308
250	12.269	0.00596	41.019	0.00599	36.892	0.00604
300	15.611	0.00806	57.738	0.00777	42.005	0.00758
350	20.037	0.00932	70.171	0.00814	47.507	0.00961

flow rates, the effect of fluid flow on the CF and contact stability at two common AFib sites was studied. Our results showed that depending on the ablation site (i.e., LIPV or RIPV) and the magnitude of the reference CF, the fluid flow could change the normal CF in the range of 25% to 48%. The change in tangential components could be even more significant. Two distinct effects were also identified: (i) catheter deflection which may compromise the force transmissibility, and (ii) fluid drag that may "lift" the catheter thus reducing the CF in flow conditions encountered in common ablation sites inside the LA. In the present experiments, for simplicity, the flow was kept steady, and a rigid chamber was used to mimic the LA. This might be considered as an acceptable quasi-steady approximation of the actual pulsatile blood flow through pulmonary veins and the LA. Future studies will include a compliant chamber since a real LA continuously undergoes expansions and contractions. Another limitation of this work was to use water to represent blood, while blood is more viscous and denser and thus could significantly increase the fluid drag. Moreover, in the present set-up, the catheter was made in contact with a rigid surface while the real atrial tissue is viscoelastic with small friction coefficients, which could further reduce the stability of the catheter in the experimented ablation sites.

Chapter 3

Physics-informed Neural Modeling of Quasi-static Soft Robots for Percutaneous Interventions

3.1 Introduction

As fully dicussed in chapter 1, Minimally Invasive Surgery (MIS) aims to reduce patient trauma, accelerate recovery, and improve surgical outcomes by replacing traditional open surgery [30, 89]. Soft continuum robots play a crucial role in minimally invasive surgery by offering unique advantages over traditional surgical tools, such as providing enhanced dexterity, flexibility, and safety. While the flexibility of soft robots allows them to navigate through unpredictable and constantly changing environments, it also poses control difficulties, particularly when interacting with anatomical structures. Given the insertion of soft robots within the human body during surgical procedures, real-time monitoring and control of both the force exerted and the shape assumed by these flexible robotic systems is essential.

The determination of shape, force, or both, is contingent upon the specific application and clinical requirements.

3.2 Materials and Methods

3.2.1 A model-based method for shape reconstruction

Equation of equilibrium

A constitutive model is used to relate the shape of a soft robot to the forces acting on it. Here, we use the Euler-Bernoulli beam theory which has two key assumptions [21]: (i) beam's cross-section is infinitely rigid within its own plane, meaning that no deformations occur in the plane of the cross-section, and (ii) during deformation, the cross-section remains plane and perpendicular to the deformed axis of the beam. The following equation gives the relationship between the applied load and the resulting deflection of a soft robot:

$$M(s) = EI\kappa, \tag{3.1}$$

where $\mathbf{M}(s)$ represents the internal bending moment at a section located at arclength distance $s \in [0, 1]$, E is Young's modulus of elasticity, I is the second moment of area of the cross-section, κ is the curvature.

Using the Frenet-Serret formula, κ can be obtained [80]:

$$\kappa = \frac{\|\mathbf{c}'(s) \times \mathbf{c}''(s)\|}{\|\mathbf{c}'(s)\|^2}, \tag{3.2}$$

in which $\mathbf{c}(s)$ denotes the position vector in the Cartesian coordinate system; prime denotes the derivative with respect to s; *cross* represents a cross product, and $||\ .\ ||$ denotes the

magnitude of a vector.

It should be noted that for a body lying in the xy-plane, i.e. $\mathbf{c}(s) = x(s)\mathbf{i} + y(s)\mathbf{j}$ ($\mathbf{i}$ and $\mathbf{j}$ being the unit vectors in the x- and y-directions, respectively), by assuming the inextensibility of the neutral axis, i.e. $x'^2 + y'^2 = 1$, equation (3.2) is reduced to the following well-known form [103]:

$$\kappa = \frac{y''}{\sqrt{1 - y'^2}}. \tag{3.3}$$

See Figure 3.1(a) which schematically shows the forces and moments that typically act on a soft robot during a minimally invasive surgery. The moment and forces acting at the robot's end manipulator are represented by $\mathbf{M}_{tip}$ and $\mathbf{F}_{tip}$, respectively. Additionally, the distributed load q (i.e., force per unit length), which may represent the effect of fluid flow (e.g., blood flow in the left atrium), is applied to the entire body of the robot. To simplify the analysis, we assume that the soft robot lies in the xy-plane, and the distributed load is downward, opposite to the direction of the y-axis. Considering a section of the soft robot at s, the equation of moment balance can be written as (see Figure 3.1(b)) follows

$$M(s)\mathbf{k} = \Big(\mathbf{c}(1) - \mathbf{c}(s)\Big) \times \mathbf{F}_{tip} + \mathbf{M}_{tip} + \mathbf{M}_q, \tag{3.4}$$

where $\mathbf{k}$ is the unit vector normal to the xy-plane; $\mathbf{M}_q$ is the bending moment due to q, which is given as below:

$$\mathbf{M}_q = \int_s^1 (\mathbf{c}(\eta) - \mathbf{c}(s)) \times (-q\mathbf{j}) \mathrm{d}\eta, \tag{3.5}$$

where η is a dummy variable.

For a stationary cylindrical body of diameter D, subjected to a fluid with density ρ, flowing with the velocity U normally to the longitudinal axis of the body, q is obtained as

$$q = \frac{1}{2}\rho U^2 D C_D, \tag{3.6}$$

where C_D is the drag coefficient which is generally dependent on the Reynolds number; however, for the range of the Reynolds number typically seen by ablation catheters in the left atrium ($100 < Re < 1000$), the drag coefficient may safely be taken in the range of $C_D \approx 1.0 - 1.2$ [12]. It should be noted that, in equation (3.6), the effects of the dynamics of the body have been neglected. Also, for simplicity of the analysis, the x-component of fluid flow forces has been neglected. This component becomes more significant as the deformations of the soft robot become larger. A future model will include both the x- and y-components of fluid flow forces.

Combining equations (3.1), (3.4) and (3.5), the governing equation in the final form can be written as

$$EI\frac{\|\mathbf{c}'(s)\times\mathbf{c}''(s)\|}{\|\mathbf{c}'(s)\|^2}\mathbf{k} = \Big(\mathbf{c}(1)-\mathbf{c}(s)\Big)\times\mathbf{F}_{tip}+\mathbf{M}_{tip}-\int_s^1(\mathbf{c}(\eta)-\mathbf{c}(s))\times(q\mathbf{j})\mathrm{d}\eta. \qquad (3.7)$$

Bézier curve approximation

Equation (3.7) is a nonlinear integro-differential equation. Similar equations have previously been developed and solved by a number of researchers. For example, [71] obtained the nonlinear equation for the large deflection of cantilever beams made of Ludwick type material, subjected to a uniformly distributed load and a tip force. The nonlinear equation was solved using Butcher's fifth-order Runge-Kutta method. [32] studied the large deflection behaviour of prismatic and non-prismatic cantilever beams subjected to generally non-uniform distributed loads and tip forces and tip moment. The nonlinear differential equation governing the deflection was obtained as a function of the angle of rotation of the beam. The solution was expressed as a polynomial in terms of the arclength of the deflected beam axis, and the unknown coefficients of the polynomial were obtained by minimizing the integral of the

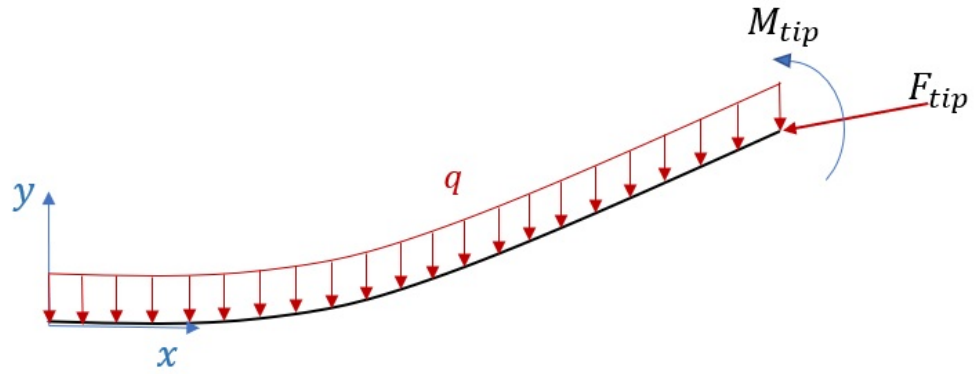

(a)

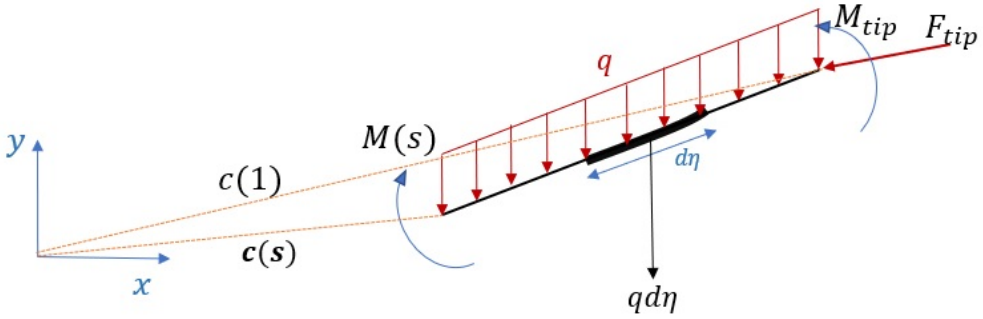

(b)

Figure 3.1: Schematic drawings showing (a) a soft robot in static equilibrium under the influence of a tip force, a tip moment and a distributed load, and (b) applying moment balance for a segment extending between $s > 0$ and $s = 1$.

residual error of the governing equation and applying the boundary conditions. [73] developed a mechanics model for large deformation of hard-magnetic soft rods with deformable cross-section. They employed the finite element method for solving the weak form of the equations.

Here, instead of solving the governing equation, we approximate the shape of the soft robot by a Bézier curve:

$$\mathbf{c}(s) \approx \mathbf{C}(s) = \sum_{i=0}^{n} \binom{n}{i} (1-s)^{n-i} s^i \mathbf{P}_i, \tag{3.8}$$

where $\mathbf{P}_i = (P_{i,x}\ P_{i,y})(\mathbf{i}\ \mathbf{j})^T$ represent the position of the control points of the Bézier curve, n is the order of the curve, and $\binom{n}{i}$ represent the corresponding binomial coefficients. Bézier curves have successfully been used in previous studies (e.g. [57], [58]) to represent the deformed shape of continuum arms/robots. Here, we adopt a cubic Bézier curve (i.e., $n = 3$) to limit the computational costs. Thus,

$$\mathbf{C}(s) = (1-s)^3\mathbf{P}_0 + 3(1-s)^2 s\mathbf{P}_1 + 3(1-s)s^2\mathbf{P}_2 + s^3\mathbf{P}_3. \tag{3.9}$$

The first and second derivatives of $\mathbf{C}(s)$ can be conveniently obtained from equation (3.9):

$$\mathbf{C}'(s) = 3(1-s)^2 (\mathbf{P}_1 - \mathbf{P}_0) + 6(1-s)s (\mathbf{P}_2 - \mathbf{P}_1) + 3s^2 (\mathbf{P}_3 - \mathbf{P}_2), \tag{3.10}$$

$$\mathbf{C}''(s) = 6(1-s) (\mathbf{P}_2 - 2\mathbf{P}_1 + \mathbf{P}_0) + 6s (\mathbf{P}_3 - 2\mathbf{P}_2 + \mathbf{P}_1). \tag{3.11}$$

Considering the simplification made above, the integro-differential equation (3.7) can be reformulated as a nonlinear algebraic equation where the uknowns would be $\mathbf{P}_i$.

Minimization problem

The resulting nonlinear algebraic equation will have a maximum of $2(n+1)$ unknowns (considering a planar configuration) while the equation can technically be used for any $s \in [0, 1]$ and thus infinite number of equations. An efficient solution to this is to re-formulate the problem as a minimization problem:

$$\min\ F = w \int_0^1 R^2 ds + (1-w) (L - L_0)^2, \tag{3.12}$$

where F represents the objective function, $R = (LHS^2 - RHS^2)$ is the difference between squared l.h.s. and r.h.s. of equation (3.7), and $0 < w < 1$ is a weight function; also, L_0 and L are the length of the soft robot before and after deformation, respectively.

In equation (3.12), the first term on the r.h.s. ensures the moment equilibrium along the soft robot while the second term works as a constraint (i.e., the soft robot is inextensible) to yield unique solutions. Assuming that the soft robot is fixed at $s = 0$, one can conclude from equation (3.9) that $P_{0,x} = P_{0,y} = 0$. In other words, the first control point must be located at $s = 0$. In addition, since at the fixed end, the slope is zero, after some mathematical manipulation, one can show that $P_{1,y} = 0$. This means that the second control point is located on the x-axis. Thus, the number of unknowns (or optimization variables) reduces from 8 to 5, for a cubic Bézier approximation.

The minimization problem is solved via MATLAB's *fminunc* function. The numerical results from the model, which essentially include deformed shapes of a beam under various loading scenarios, are compared with FEM results obtained via Abaqus. All the numerical results were obtained with a desktop which has an Intel core i7-4790 (3.6 GHz) processor and 20 GB of installed RAM.

3.2.2 A learning-based model for shape reconstruction

As shown in Section 3.2.1, a model-based method capable of obtaining the shape of a soft robot was developed. However, one major drawback of this method is its relatively high computational time, which hinders its use in actual clinical applications where real-time response is required.

Here, we develop a learning-based model with the hope that such a model can potentially run much faster. The model is developed using the Bayesian Neural Network (BNN) and employing 10 hidden layers. BNN is a type of neural network that incorporates Bayesian

inference to model uncertainty in the network's parameters. In contrast to standard neural networks, the weights and biases in the BNN do not take unique values but have probability distributions attached to them [83]. BNN is chosen due to the vulnerability of traditional neural networks to overfitting where training data memorization occurs, resulting in inadequate performance with unseen data. In contrast, BNNs provide plausible explanations for training data, transcending mere data fitting. This strategy mitigates overfitting risks and promotes improved generalization [24].

The required data for training, testing and validating the neural network is provided by the model-based method of Section 3.2.1. A total of 1296 cases were run, 70% of which are used for training, 15% are used for validation, and the remaining 15% are used for testing. The inputs are the tip force components ($0 \leq f_x, f_y \leq 0.5$ N), the tip moment ($0 \leq M \leq 5$ N.mm), and the force per unit length due to fluid flow ($0 \leq q \leq 0.5$ N/m) while the outputs are the coordinates of the Bézier curve control points, i.e., $P_{1,x},\ P_{2,x},\ P_{2,y},\ P_{3,x},$ and $P_{3,y}$; see Figure 3.2. The range of values taken for the input variables are typical of ablation catheters in the left atrium.

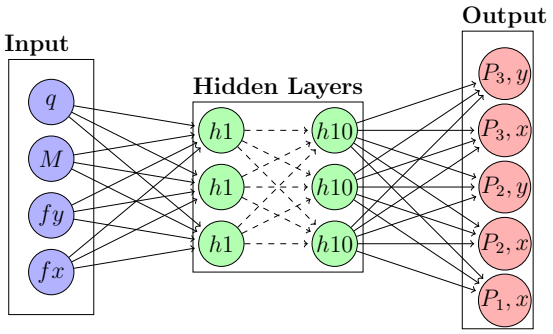

Figure 3.2: Schematic of the neural network used for shape reconstruction.

3.2.3 A learning-based model for force estimation

There is a growing interest in the medical research community to develop sensorless or sensor-free surgical robot technologies with the aim of significantly reducing the cost of such devices and thus the surgical procedure. Sensorless ablation catheters, for example, need reliable real-time tip-force estimations. This need has motivated us to develop a second learning-based model which will be used for tip force estimation. Here, the inputs include the shape of the robot (i.e., the coordinates of the Bézier curve control points) which can be obtained from, for example, fluoroscopic images, the tip moment applied by the surgeon via a handset or a controlling knob, and the distributed load due to blood flow, which may be obtained from *in vitro* measurements or computational fluid dynamic simulations. The outputs, on the other hand, include the components of the tip force; see Figure 3.3.

The same algorithm and number of hidden layers as those in Section 3.2.2 are used here. In addition, the same proportion of cases as those in the previous section are used here for the training, validation and testing.

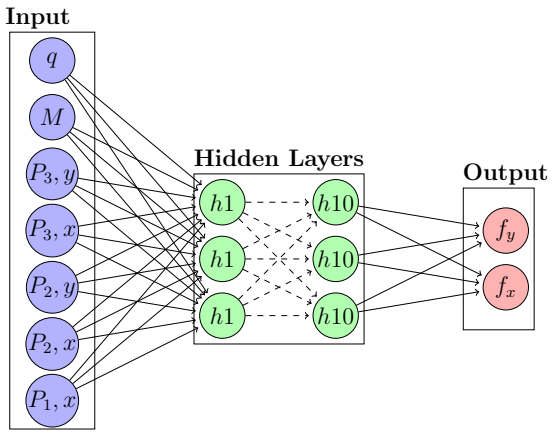

Figure 3.3: Schematic of the neural network used for force estimation.

3.2.4 *In vitro* experiments

Some *in vitro* experiments were conducted by the authors [64] with the aim of examining the effects of fluid flow on the tip force of ablation catheters. The results from one set of these experiments will be used for comparison against the numerical results from the learning-based model of Section 3.2.3.

Experimental apparatus

Figure 3.4 shows the components of a closed-loop experimental setup designed to replicate blood circulation during the ablation procedure — a minimally invasive surgery conducted within the left atrium of heart to treat arrhythmia. In order to simulate this procedure, an 8-Fr (1 Fr $\sim$ 1/3 mm) Ablation Catheter (Blazer II XP, Boston Scientific, MA, USA) was employed as a representative example of a soft robot. Additionally, four Digiten G3/8 Hall sensors were utilized for flow rate measurement. These flow sensors were calibrated against a standard flow meter (Cole Parmer, IL, USA). Interrogation of the flow meters was carried out using an Arduino Mega 2560 with custom-developed firmware programmed in C++. Furthermore, a six-axis Force/Torque sensor (Mini40, ATI Industrial Automation, NC, USA) was employed for measuring the force exerted at the catheter tip. Water was used as the working fluid, which was circulated using two Deluxe 1056 GPH submersible pumps. 3-D printed parts were used to enclose the valves, flow meters as well as to support the catheter.

As seen from the figure, water was pumped from a reservoir and was divided into four branches, each leading to a pulmonary vein through which the flow entered the chamber. The flow in the branches was manually adjusted using four needle valves. The setup could accommodate flow rates up to 350 LPH (liters per hour) in each branch. The direction and

velocity of the flowing water accurately followed the physiological conditions. For simplicity, a cylindrical chamber was chosen instead of a chamber with the exact geometry and dimensions of the left atrium. The fluid within the chamber was drained through a hole located at the bottom of the chamber, which matched the size of the mitral orifice of the left atrium based on anatomical references. As also seen from the figure, an orifice was made on the lateral surface of the chamber opposite to the pulmonary veins (simulating a transseptal puncture) to allow for the passage of the catheter. This orifice was sealed using an 8-Fr introducing sheath. Since the force sensor was not water resistant, force measurement was done indirectly. An L-shaped rod was designed and 3D-printed to transmit the force from inside the chamber to the outside. This rod, acting as a force transmitter, was securely attached at one end to the force sensor. At the other end, the force transmitter was placed in close proximity to (but not in contact with) the inner lateral surface of the chamber and in contact with the tip of the catheter.

3.3 Results and discussion

3.3.1 Validation of the model-based method for shape reconstruction

To assess the accuracy of the model-based method proposed in Section 3.2.1, a comparative study is performed against a finite element method (FEM) model created in Abaqus. More precisely, the deformed shape of a soft robot, which is represented as a cantilevered beam of length $L = 40$ mm and flexural rigidity $EI = 750$ N.mm^2, was obtained for various loading cases, using the present model and the FEM model. Six loading cases were selected from many, which are shown schematically in Figure 3.5. As seen, these six cases include a good

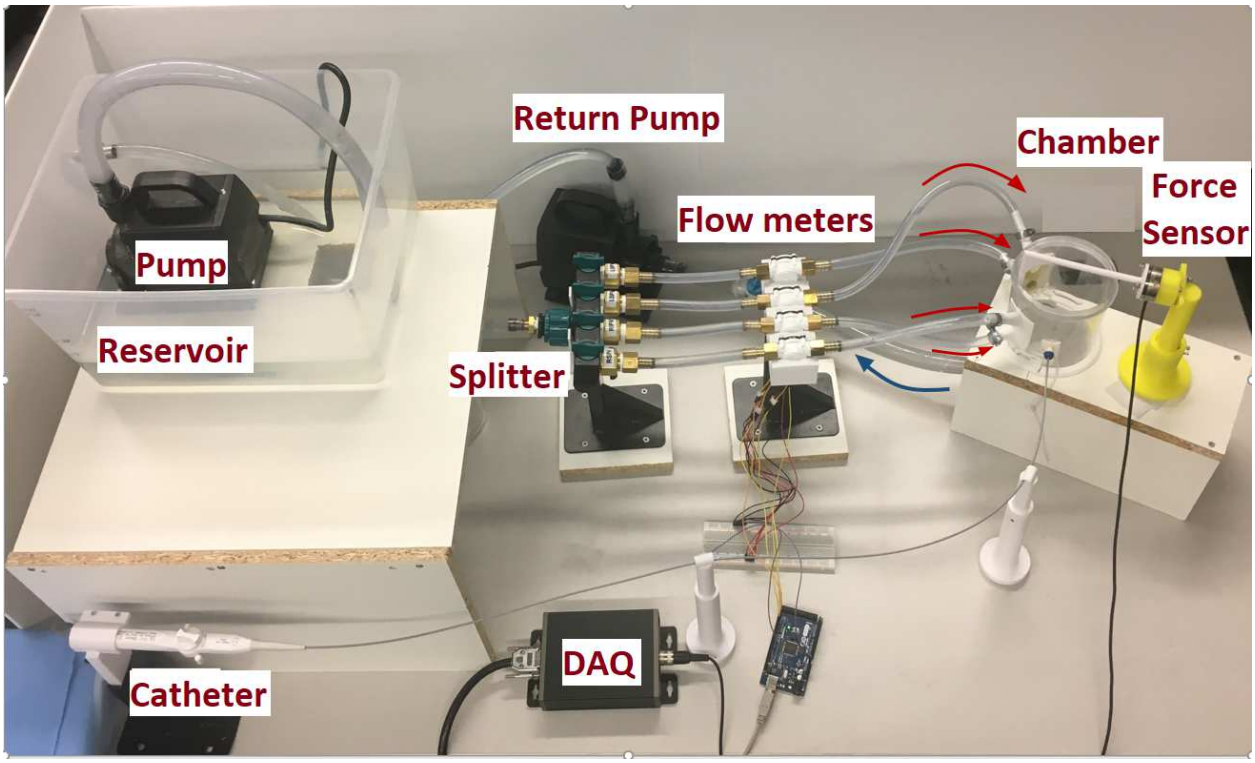

Figure 3.4: Experimental apparatus for examining the effects of fluid flow on the force acting on the tip of ablation catheters. In the figure, red arrows show the flow direction from the reservoir to the chamber while the blue arrow shows the flow direction from the chamber back to the reservoir [64].

mix of tip forces, tip moment, and distributed load.

Figure 3.5 shows the comparison between the deformed shapes obtained from the proposed model (represented by solid lines) and those obtained from the FEM model (represented by markers). Overall, a very good agreement is observed between the results from the two models, even when deformations are large, such as in case 3 or case 6. A quantitative comparison is also made, where the tip displacement of the beam in the x- and y-directions, obtained from the two models are compared; see Table 3.1. As seen, the error for the x-component of the tip displacement is around 2% and that for the y-component is below 5%. Generally, a higher error is observed when the deformation is larger. From the results, one may conclude that the model based on the 3rd-order (or cubic) Bézier curve may be still

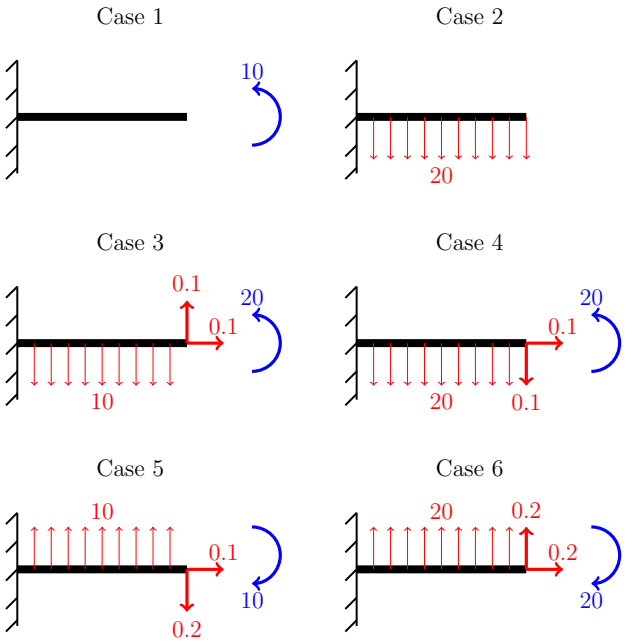

(a)

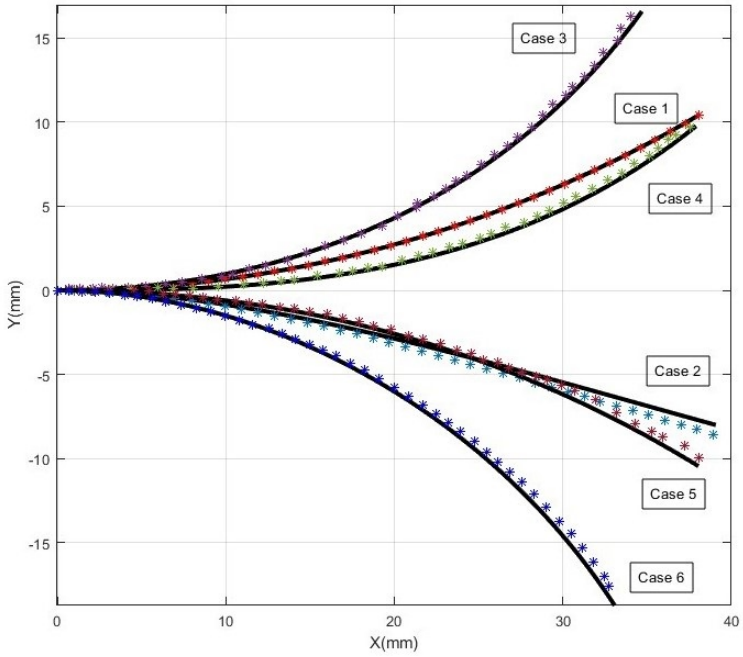

(b)

Figure 3.5: Validation of the model-based method: (a) six different load cases, and (b) comparison between deformed shapes obtained from the present model (solid line) and those from the FEM model (markers).

Table 3.1: Tip displacement of a cantilevered Euler-Bernoulli beam ($EI = 750$ N.mm^2, $L = 40$ mm) for the load cases shown in Figure 3.5. The column called 'Bézier' provides the numerical values obtained from the model-based method while the column called 'FEM' gives the results from Abaqus.

Case	**Loads**				**Tip displacement x (mm)**			**Tip displacement y (mm)**		
	f_x (N)	f_y (N)	M (N.mm)	q (N/m)	Bézier	FEM	Error %	Bézier	FEM	Error %
1	0	0	10	0	38.12	38.13	0.03	10.43	10.42	-0.10
2	0	0	0	-20	39.02	38.94	-0.21	-8.59	-8.56	-0.35
3	0.1	0.1	20	-10	34.70	34.01	-2.03	16.59	16.25	-2.09
4	0.1	-0.1	20	-20	37.91	37.55	-0.96	9.76	9.71	-0.51
5	0.1	-0.2	-10	10	38.05	37.22	-2.23	-10.45	-9.99	-4.60
6	0.2	0.2	-20	-20	33.33	32.76	-1.74	-19.13	-18.22	-4.99

reliable even when the tip displacement of the robot is almost 50% of the length while for larger displacements, a higher-order Bézier curve should be employed in the modeling to ensure accuracy.

Using the model, the average run-time for a case was approximately 0.9 s (equivalent to ~ 1 Hz) which is far from the requirement of 10-30 Hz for the use in clinical applications [75]. Thus, despite the reasonable level of accuracy demonstrated by the model, it is not ready yet for the use in real-world scenarios.

3.3.2 Numerical results from the learning-based model for shape reconstruction

Table 3.2 provides the results from training, validation, and testing the learning-based model for shape reconstruction, described in Section 3.2.2. As seen, the mean squared error (MSE) is always in the order of 10^{-5}. In addition, the correlation coefficient R is very close to 1, which indicates a strong linear relationship between predicted and target values. Both these measures confirm the accuracy of the model.

Figure 3.6 shows the variation of the MSE as a function of the number of epochs for both the training and testing phases. An epoch refers to the training the neural network (NN)

Table 3.2: Mean squared error (MSE) and correlation coefficient (R) for training, validation and testing the BNN for shape reconstruction.

		MSE	R
# Train	908	6.8161e-5	0.9996
# Validation	194	5.0733e-5	0.9998
# Test	194	3.3425e-5	0.9999

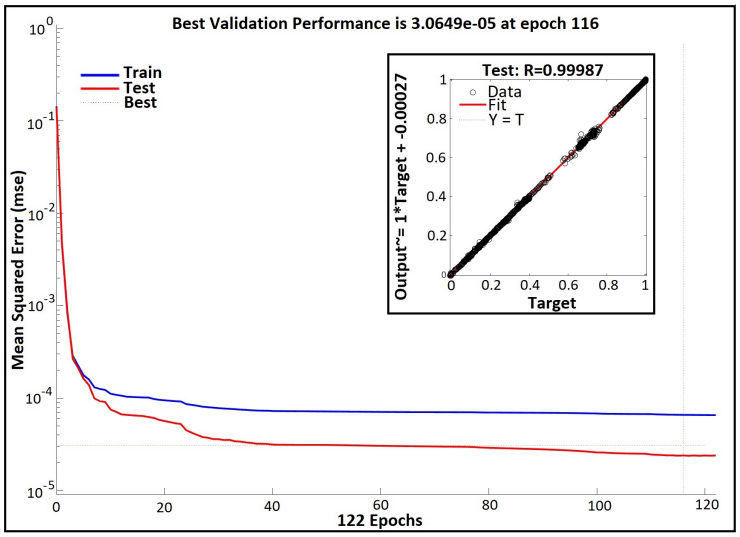

Figure 3.6: Evolution of the mean squared error during training and testing of the shape reconstruction NN model. The inset shows the correlation between predicted and target values.

with the entire training data for one cycle. As seen from the figure, the MSE for testing (red, online) goes below 10^{-4}, relatively fast (i.e., after first few epochs). The MSE for training (blue, online) reaches almost a plateau after 40 epochs. Interestingly, the MSE of the test data is almost always below that of the train data. This means that the NN performs even better on unseen data. The inset to the figure shows the quality of the fitness of the model predictions to the target values. As seen, the predictions fit very well to the target values.

The average run-time for the NN model was found to be approximately 0.02 s (equivalent to 50 Hz) which is even above the required range for clinical applications. Given that the model is both accurate and fast, it is suitable for the use in real-world scenarios.

3.3.3 Numerical results from the learning-based model for force estimation

Table 3.3 provides the values of the MSE and R for training, validation and testing the learning-based model for force estimation, described in Section 3.2.3. As seen, the MSE is in the order of 10^{-5} in all the three phases, which is an order of magnitude higher than the MSE values obtained for the shape reconstruction model (cf. Table 3.2). The MSE slightly increases from training to testing, which is a quite common behaviour. The correlation coefficient R is also fairly close to 1, which confirms a strong linear relation between predicted and target values. Both MSE and R values confirm the accuracy of the learning-based model for force estimation.

Figure 3.7 shows the evolution of the MSE as the number of epochs is increased. As seen, much more number of epochs are required to converge to an acceptable accuracy when compared to the model in Section 3.3.2. The inset also indicates a fairly good linear correlation between predicted and target values.

Table 3.3: Mean squared error (MSE) and correlation coefficient (R) for train, validation and test of the BNN for force estimation.

		MSE	R
# Train	908	1.3741e-5	0.9992
# Validation	194	1.5443e-5	0.9991
# Test	194	1.9129e-5	0.9990

Comparison with in vitro experiments

The experimental apparatus described in Section 3.2.4 was employed to measure the tip force of the catheter (at the contact point between the catheter and the force transmitter) at different flow rates. These measurements are compared against predictions made by the

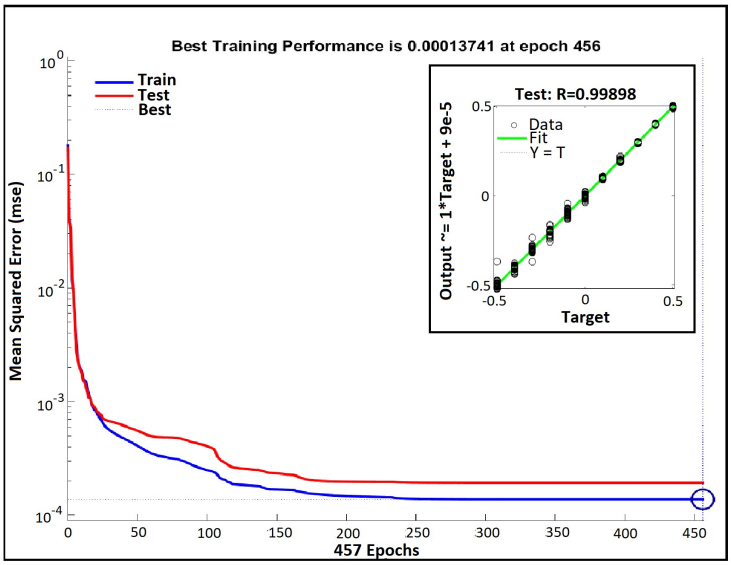

Figure 3.7: Evolution of the mean squared error during training and testing of the force estimation NN model. The inset shows the correlation between predicted and target values.

learning-based model.

Figure 3.8(a) shows a top-view of the chamber. As seen, the tip of the catheter is in contact with the tip of the force transmitter which has been placed in the vicinity of the left inferior pulmonary vein. This is a common ablation area during actual operations. In this experiment, the flow into the chamber is only through the right inferior pulmonary vein. Four different flow rates 200, 250, 300, and 350 LPH were tested. The selection of these flow rate values is grounded in the actual blood flow rate entering the left atrium through the four inlets known as pulmonary veins [70] and the value of M_{tip} is 12 N.mm^2. Before doing measurements for different water flow rates, the contact force was measured when the chamber was empty, i.e. the contact force in the air. Ideally, the deformed shape of the catheter had to be taken in air and for all four flow rates. However, only the deformed shape of the catheter in the air could be retrieved from the stored data. Given that the shape of the catheter does not significantly change due to the flow, this same image will be used for all the cases.

The shape of the catheter was extracted using PlotDigitizer from the image shown in Figure 3.8(a). The digitized shape is represented by a blue curve in Figure 3.8(b). Using MATLAB, a cubic Bézier curve was fitted to the digitized shape, which is represented by a green curve in the figure. As seen, the quality of the fitting is quite well close to the tip of the catheter while it might be possible to improve it close to the fixed end using a higher-order Bézier curve. Nevertheless, this is beyond the scope of the present work and is deferred to a future study. The forces acting at the tip of the catheter are normal and tangential to the tip. These forces are represented by $F_{y,exp}$ and $F_{z,exp}$, respectively. The forces and the flow direction are described in the coordinate system attached to the catheter, as shown in Figure 3.8(c).

Figure 3.9 shows the comparison between experimentally measured and numerically obtained tip force in air and in the presence of fluid flow. The figure shows the variation of (a) f_x, and (b) f_y as a function of the flow rate. Considering the experimental results, both f_x and f_y are decreased as the flow rate is increased. This can be understood when considering the direction of flow with respect to the direction of tip force. For example, f_x has a positive value in air; a flow with the direction shown in Figure 3.9(c) will generate a force in the x-direction, the reaction of which would be acting at the tip in the opposite direction. Thus, f_x in the presence of fluid flow would be smaller than f_x in air. As the flow rate is increased, the fluid flow force and thus the opposing reaction force become stronger, and as a result, f_x is further reduced.

As also seen from the figure, f_x and f_y obtained form the learning-based model follow a similar trend as observed form experimental results. Interestingly, the model always overestimates f_x and f_y. As the flow rate is increased, the difference between experimental and numerical values becomes smaller.

Table 3.4 provides a more detailed quantitative comparison between experimental and

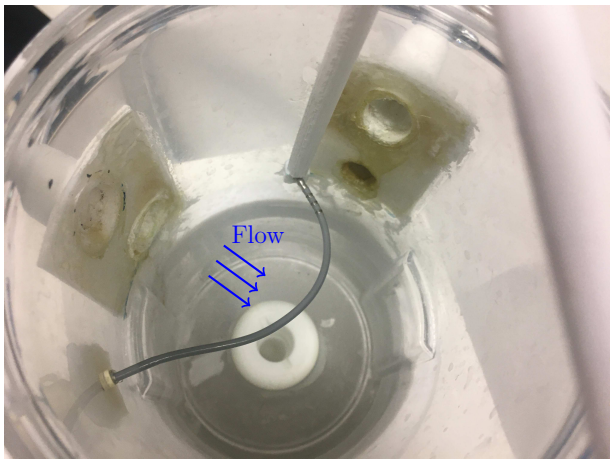

(a)

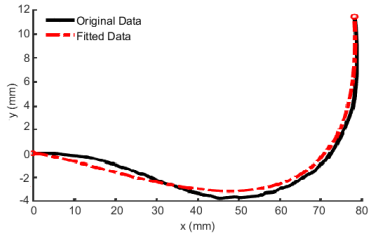

(b)

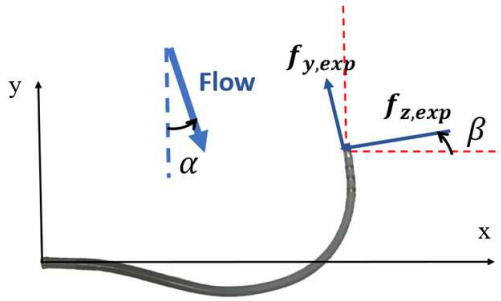

(c)

Figure 3.8: In vitro experiments used for the validation of the force estimation NN model: (a) top-view of the chamber, showing the position of the tip of the catheter and the flow direction, (b) the digitized shape of the catheter (black) versus the fitted curve (dashed red), and (c) the forces measured by the force sensor ($f_{y,exp}$ and $f_{z,exp}$) and the flow direction, described in the Cartesian coordinate system attached to the catheter, (x, y); the angles are: $\alpha = 35°$, and $\beta = 40°$.

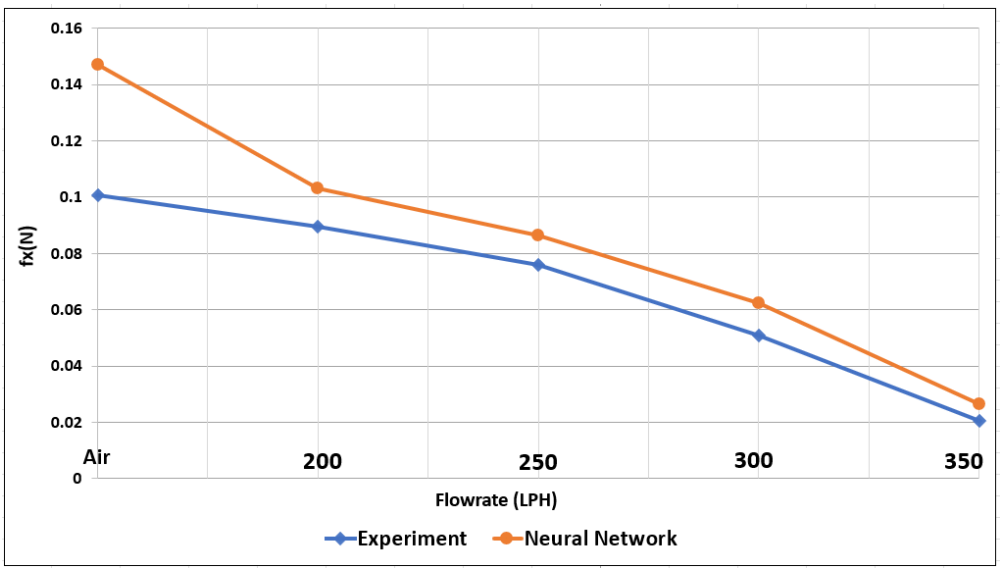

(a)

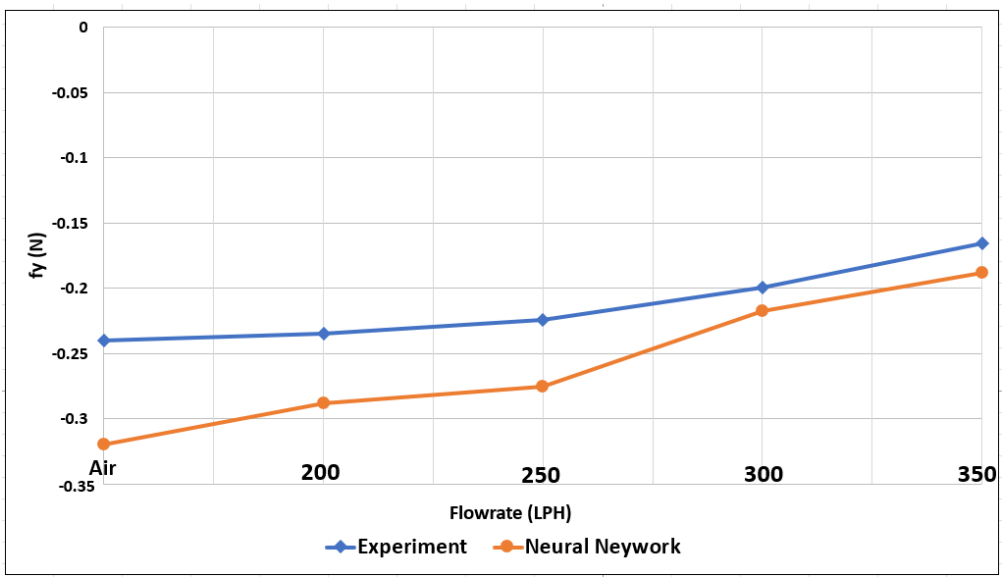

(b)

Figure 3.9: Comparison between tip force components measured experimentally via a force sensor (blue) and those estimated using the force estimation NN model (orange) for no flow (air) as well as four different flow rates.

numerical results. Both absolute values of the tip force components f_x and f_y, as well as relative errors $\delta_x = 100 \times (f_{x,NN} - f_{x,exp})/f_{x,exp}$ and $\delta_y = 100 \times (f_{y,NN} - f_{y,exp})/f_{y,exp}$ were

Table 3.4: Comparison between experimental and numerical values from the force estimation NN model; f_x and f_y are the tip force components in the x- and y-directions, respectively; δ_x and δ_y represent the relative errors between the two sets for f_x and f_y, respectively.

			Flow Rate (LPH)			
	Tip force (N)	No flow (air)	200	250	300	350
Experiment	$f_{x,exp}$	0.1007	0.0894	0.0759	0.0509	0.0204
	$f_{y,exp}$	-0.2399	-0.2343	-0.2238	-0.1991	-0.1658
Neural Net.	$f_{x,NN}$	0.1714	0.1032	0.0863	0.0625	0.0263
	$f_{y,NN}$	-0.3198	-0.2882	-0.2754	-0.2174	-0.1881
Rel. Error (%)	δ_x	46.07	15.49	13.59	22.65	28.61
	δ_y	33.29	22.99	23.05	9.20	13.43

reported. As seen, except for the results in air, the learning-based results are within 30% of the experimental results. Overall, a better agreement is seen for f_y values. Given that the NN model has been trained using the data obtained from a theoretical model (and not actual experimental data), the level of agreement is fair. Several sources of uncertainty exist in the theoretical model, which could be the reason for the discrepancy between experimental and numerical results. For example, the flow field inside the chamber is highly uncertain. The flow expands upon entering the chamber, it is confined, and complex vortical structures are likely to exist. All these combined, make the flow velocity (and thus the fluid force) magnitude, direction, and distribution non-uniform. In contrast, in the theoretical model, the force due to fluid flow was assumed to be in a fixed direction and uniformly distributed over the catheter. Another source of uncertainty and a likely reason for the discrepancy is how much the shape of the catheter varied with the variation of the flow rate. As discussed previously, a single image (deformed shape in air) was fed to the NN model regardless of the flow rate.

3.4 Conclusions

The present study developed two novel, physics-informed neural network models that hold significant potential for various applications in the field of soft robotics, particularly in minimally invasive surgery. The first model could accurately (MSE $\sim 10^{-5}$) and quickly (refresh rate $\sim$ 50 Hz) reconstruct the shape of the inserted robot within the body when the information on the tip force, tip moment, and distributed load due to fluid flow are fed to the model. Such a model could potentially obviate the need for medical imaging during operations, thus making them safer and more affordable. The second NN model offered the ability to predict forces based on the shape of the robot (i.e., artificial force sensing), making it highly valuable in applications where precise force control is critical. Such a model could greatly contribute to the development of sensorless or sensor-free technologies which again aim to reduce the cost of surgical operations. The results from this model were compared with those from a one-of-a-kind experimental apparatus developed to examine the effects of fluid flow on ablation catheters. The two sets of results were similar in trend while the relative error was found to be in the range of 9-46%.

The data needed for training, validation, and testing the two NN models was collected from solving a novel theoretical model. The novelty mainly lies in the inclusion of fluid flow effects, which had been largely neglected in previous studies despite their substantial significance. The theoretical model was developed based on the Euler-Bernoulli beam theory, employing the moment balance equation, and the use of cubic Bézier curve to approximate the shape of the soft robot. The resulting equations were solved through a minimization approach. The results from the theoretical model were validated against those from a finite element model, with a maximum relative error below 5%.

Considering the real-time nature of shape and force control requirements in minimally

invasive surgery, the two NN models hold the potential to serve as versatile tools for addressing various medical needs. Moving forward, further improvements to the models are anticipated. For example, a fresh experimental campaign will be conducted to collect test data for training the NN models more comprehensively. In addition, the theoretical model will be improved, for example, by using higher-order Bézier curves for shape approximation, which eventually help to get more accurate NN models. By making such improvements, significant contributions are expected to the advancement of the field of soft robotics in medical applications.

Chapter 4

Conlcusion and Future works

4.1 Conclusions

This thesis brings together two important studies concerning medical applications. The first study focused on the experimental examination of the fluid effects on catheters in the left atrium of the heart. By testing catheters in varying flows, we learned that fluid dynamics can change forces on the catheters, sometimes by a large amount. It was found that, depending on the location of the tip of catheter (i.e. the ablation site) and the prevalent flow direction, the fluid flow may reduce or increase the no-flow contact force. And this negatively affects both the efficiency and stability of the contact (or tip) force in the ablation procedure. The results from the experimental study indicated the importance of including fluid flow forces in the mechanistic models developed for shape reconstruction or tip-force estimation.

In the second study, two novel neural network based models were developed for soft robots in contact with fluid flow. One model could recreate a robot's shape in real time, given the loads acting on it.Such a model can potentially obviate the need for imaging, thereby mitigating health risk due to exposure to medical scans in surgical applications.

The other model could do real-time force estimation. This type of models can significantly contribute to the development of sensorless soft robots which are expected to be very cost effective. Comparing the models with real tests showed they're promising for real-world use.

Behind all this progress was a new mechanistic model took into account the effect of fluid flow. The model was validated against a finite element model. Although the model was reasonably accurate, it was not real-time fast. considering the typical range of forces and fluid flow in the ablation procedure, a fairly good amount of data was created via the model, which was then used for developing NN based models. Developing more accurate mechanistic models could potentially leads to the development of more reliable NN based model.

We see how these studies fit into the fast pace of surgerical advancement. Our models could help make surgeries safer and more effective. Looking forward, we plan to make our models even better by collecting more data and refining our theory, and excited about what lies ahead in the world of medical robotics.

4.2 Future Work

Herein are presented several recommendations for prospective endeavors that may extend the trajectory of my research in a supplementary manner.

In the context of the initial phase, it is proposed that subsequent investigations could be pursued:

- The chamber utilized in the experiments did not accurately represent the mechanical properties and the geometry of the left atrium. Consequently, in the forthcoming phase of the investigation, a flexible chamber which also precisely emulates the left atrium's geometry will be used. This approach can increase the level of realism in fluid

dynamics, resulting in more accurate findings.

- The flow was maintained in a steady-state condition as a simplification measure. To enhance the accuracy of the flow representation, it is suggested that a pulsatile flow, akin to the human body's circulatory rhythm, be introduced into the system. This approach aims to bring the setup closer to the physiological conditions of the actual human body.

In the context of the second part of this research, the following studies may be put forth as a progression of my work:

- In cases where soft robots experience significant deformation and intricate forces and moments, employing higher order Bézier curves becomes essential for enhanced precision. While this may lead to increased computational requirements, the growing dataset, when trained using neural network methods, has the potential to alleviate this complexity.

- The methodology can identically be extended into a three-dimensional framework, advancing our alignment with the physiological complexities of the human body. In this context, all three equations governing moment equilibrium possess non-trivial values, demanding their concurrent resolution and rigorous validation.

References

[1] Continuum robot. https://www.cardion.cz/file/169/Hansen%20Medical%20brochure-EU.pdf. Accessed: 2023-08-01.

[2] Minimally invasive surgery. https://medmovie.com/library_id/3255/topic/ahaw_0182i/. Accessed: 2023-07-01.

[3] Soft endoscope. https://kclhammerlab.com/2018/research/soft-self-propelled-endoscopic-robot/. Accessed: 2023-08-01.

[4] soft grasper. https://softroboticstoolkit.com/book/sdm-case-study. Accessed: 2023-08-01.

[5] H. Abidi, G. Gerboni, M. Brancadoro, J. Fras, A. Diodato, M. Cianchetti, H. Wurdemann, K. Althoefer, and A. Menciassi. Highly dexterous 2-module soft robot for intra-organ navigation in minimally invasive surgery. *The International Journal of Medical Robotics and Computer Assisted Surgery*, 14(1):e1875, 2018.

[6] A. A. Abushagur, N. Arsad, M. Ibne Reaz, A. Ashrif, and A. Bakar. Advances in bio-tactile sensors for minimally invasive surgery using the fibre bragg grating force sensor technique: A survey. *Sensors*, 14(4):6633–6665, 2014.

[7] Y. Adagolodjo, F. Renda, and C. Duriez. Coupling numerical deformable models

in global and reduced coordinates for the simulation of the direct and the inverse kinematics of soft robots. *IEEE Robotics and Automation Letters*, 6(2):3910–3917, 2021.

[8] C. C. Aggarwal et al. Neural networks and deep learning. *Springer*, 10(978):3, 2018.

[9] O. Al-Ahmad, M. Ourak, J. Vlekken, E. Lindner, and E. Vander Poorten. Three-dimensional catheter tip force sensing using multi-core fiber bragg gratings. *Frontiers in Robotics and AI*, 10:1154494, 2023.

[10] M. Alam, R. Young, and R. Diaz-Nieto. Robotic liver surgery. In S. Küçük, editor, *Latest Developments in Medical Robotics Systems*, chapter 2. IntechOpen, Rijeka, 2021.

[11] T. Amadeo, D. Van Lewen, T. Janke, T. Ranzani, A. Devaiah, U. Upadhyay, and S. Russo. Soft robotic deployable origami actuators for neurosurgical brain retraction. *Frontiers in Robotics and AI*, 8:731010, 2022.

[12] J. D. Anderson. *Fundamentals of Aerodynamics*. New York, NY: McGraw Hill, sixth edition, 2017.

[13] M. Antonilli, V. Sevas, M. L. Gasparri, A. A. Farooqi, and A. Papadia. Minimally invasive surgery in gynecology. In *Advances in Minimally Invasive Surgery*. IntechOpen, 2021.

[14] C. Appiah, C. Arndt, K. Siemsen, A. Heitmann, A. Staubitz, and C. Selhuber-Unkel. Living materials herald a new era in soft robotics. *Advanced Materials*, 31(36):1807747, 2019.

[15] J. Back, L. Lindenroth, R. Karim, K. Althoefer, K. Rhode, and H. Liu. New kinematic multi-section model for catheter contact force estimation and steering. In *2016*

IEEE/RSJ International Conference on Intelligent Robots and Systems (IROS), pages 2122–2127. IEEE, 2016.

[16] J. Back, L. Lindenroth, K. Rhode, and H. Liu. Three dimensional force estimation for steerable catheters through bi-point tracking. *Sensors and Actuators A: Physical*, 279:404–415, 2018.

[17] J. Back, T. Manwell, R. Karim, K. Rhode, K. Althoefer, and H. Liu. Catheter contact force estimation from shape detection using a real-time cosserat rod model. In *2015 IEEE/RSJ International Conference on Intelligent Robots and Systems (IROS)*, pages 2037–2042. IEEE, 2015.

[18] Z. Bai, X. Cao, B. Xiong, Y. Dong, X. Sun, and W. Sun. Clinical effectiveness of distal metatarsophalangeal mini-invasive osteotomy on hallux valgus. 2023.

[19] N. Bandari, J. Dargahi, and M. Packirisamy. Tactile sensors for minimally invasive surgery: A review of the state-of-the-art, applications, and perspectives. *Ieee Access*, 8:7682–7708, 2019.

[20] J. Bao, W. Chen, and J. Xu. Kinematics modeling of a twisted and coiled polymer-based elastomer soft robot. *IEEE Access*, 7:136792–136800, 2019.

[21] O. A. Bauchau and J. I. Craig. Euler-bernoulli beam theory. *Structural analysis*, pages 173–221, 2009.

[22] R. Berthold, M. N. Bartholdt, M. Wiese, S. Kahms, S. Spindeldreier, and A. Raatz. A preliminary study of soft material robotic modelling: Finite element method and cosserat rod model. In *2021 9th International Conference on Control, Mechatronics and Automation (ICCMA)*, pages 7–13. IEEE, 2021.

[23] M. Bijjawara, U. Bidre, and S. Vijay. Minimally invasive spine surgery: Hurdles to be crossed. *Indian Journal of Neurosurgery*, 3(01):008–013, 2014.

[24] D. Bonnet, T. Hirtzlin, A. Majumdar, T. Dalgaty, E. Esmanhotto, V. Meli, N. Castellani, S. Martin, J.-F. Nodin, G. Bourgeois, et al. Bringing uncertainty quantification to the extreme-edge with memristor-based Bayesian neural networks. *Preprint, Research Square*, 2023.

[25] F. Bourier, C. Gianni, M. Dare, I. Deisenhofer, G. Hessling, T. Reents, S. Mohanty, C. Trivedi, A. Natale, and A. AL-AHMAD. Fiberoptic contact-force sensing electrophysiological catheters: how precise is the technology? *Journal of cardiovascular electrophysiology*, 28(1):109–114, 2017.

[26] K. Chen, J. Zhang, N. M. Beeraka, M. Y. Sinelnikov, X. Zhang, Y. Cao, and P. Lu. Robot-assisted minimally invasive breast surgery: Recent evidence with comparative clinical outcomes. *Journal of Clinical Medicine*, 11(7):1827, 2022.

[27] P. Chen, Y. Yu, and Y. Liu. Variable curvature modelling method of continuum robots with contraints. 2021.

[28] Y. Chen, L. Li, W. Li, Q. Guo, Z. Du, and Z. Xu. Chapter 2 - fundamentals of neural networks. In Y. Chen, L. Li, W. Li, Q. Guo, Z. Du, and Z. Xu, editors, *AI Computing Systems*, pages 17–51. Morgan Kaufmann, 2024.

[29] D. Coban, S. Changoor, S. Saela, K. Sinha, K. Hwang, M. Faloon, and A. Emami. Obesity does not adversely affect long-term outcomes of minimally invasive transforaminal lumbar interbody fusion: a matched cohort analysis. *Orthopedics*, 45(4):203–208, 2022.

[30] M. V. Corniola, B. Debono, H. Joswig, J.-M. Lemée, and E. Tessitore. Enhanced

recovery after spine surgery: review of the literature. *Neurosurgical focus*, 46(4):E2, 2019.

[31] E. M. P. Cosserat and F. Cosserat. *Théorie des corps déformables*. A. Hermann et fils, 1909.

[32] M. Dado and S. Al-Sadder. A new technique for large deflection analysis of non-prismatic cantilever beams. *Mechanics research communications*, 32(6):692–703, 2005.

[33] A. B. Dawood, H. Godaba, and K. Althoefer. Silicone based capacitive e-skin sensor for soft surgical robots. In *Towards Autonomous Robotic Systems: 21st Annual Conference, TAROS 2020, Nottingham, UK, September 16, 2020, Proceedings 21*, pages 62–65. Springer, 2020.

[34] C. Della Santina, A. Bicchi, and D. Rus. On an improved state parametrization for soft robots with piecewise constant curvature and its use in model based control. *IEEE Robotics and Automation Letters*, 5(2):1001–1008, 2020.

[35] S. O. Demir, U. Culha, A. C. Karacakol, A. Pena-Francesch, S. Trimpe, and M. Sitti. Task space adaptation via the learning of gait controllers of magnetic soft millirobots. *The International journal of robotics research*, 40(12-14):1331–1351, 2021.

[36] A. Di Maro, S. Creaco, M. Albini, M. Latiff, and M. Merlo. Radiographic results on acetabular cup placement with the superpath technique: a retrospective study of 756 cases. *BMC Musculoskeletal Disorders*, 23(1):101, 2022.

[37] S. Dietsch, A. McDonald-Bowyer, E. Dimitrakakis, J. M. Coote, L. Lindenroth, A. Stilli, and D. Stoyanov. Localization of interaction using fibre-optic shape sensing in soft-robotic surgery tools. In *2022 IEEE/RSJ International Conference on Intelligent Robots and Systems (IROS)*, pages 8057–8063. IEEE, 2022.

[38] C. Donkor, A. Gonzalez, M. R. Gallas, M. Helbig, C. Weinstein, and J. Rodriguez. Current perspectives in robotic hernia repair. *Robotic Surgery: Research and Reviews*, pages 57–67, 2017.

[39] W. Duan, T. Akinyemi, W. Du, J. Ma, X. Chen, F. Wang, O. Omisore, J. Luo, H. Wang, and L. Wang. Technical and clinical progress on robot-assisted endovascular interventions: A review. *Micromachines*, 14(1):197, 2023.

[40] K. M. El Dine, J. Sanchez, J. A. Corrales, Y. Mezouar, and J.-C. Fauroux. Force-torque sensor disturbance observer using deep learning. In *Proceedings of the 2018 International Symposium on Experimental Robotics*, pages 364–374. Springer, 2020.

[41] J.-H. Eum, J.-H. Park, K.-S. Song, S.-M. Lee, D.-W. Suh, and D.-J. Jo. Endoscopic extreme transforaminal lumbar interbody fusion with large spacers: a technical note and preliminary report. *Orthopedics*, 45(3):163–168, 2022.

[42] I. Floris, J. M. Adam, P. A. Calderón, and S. Sales. Fiber optic shape sensors: A comprehensive review. *Optics and Lasers in Engineering*, 139:106508, 2021.

[43] E. Franco, D. Rodríguez Muñoz, R. Matía, A. Hernández-Madrid, I. Sánchez Pérez, J. L. Zamorano, and J. Moreno. Contact force-sensing catheters: performance in an ex vivo porcine heart model. *Journal of Interventional Cardiac Electrophysiology*, 53:141–150, 2018.

[44] K. C. Galloway, Y. Chen, E. Templeton, B. Rife, I. S. Godage, and E. J. Barth. Fiber optic shape sensing for soft robotics. *Soft robotics*, 6(5):671–684, 2019.

[45] J. Garcia, H. Sheitt, M. S. Bristow, C. Lydell, A. G. Howarth, B. Heydari, F. S. Prato, M. Drangova, R. E. Thornhill, P. Nery, et al. Left atrial vortex size and

velocity distributions by 4d flow mri in patients with paroxysmal atrial fibrillation: Associations with age and cha2ds2-vasc risk score. *Journal of Magnetic Resonance Imaging*, 51(3):871–884, 2020.

[46] P. C. Giulianotti, F. Sbrana, F. M. Bianco, E. F. Elli, G. Shah, P. Addeo, G. Caravaglios, and A. Coratti. Robot-assisted laparoscopic pancreatic surgery: single-surgeon experience. *Surgical endoscopy*, 24:1646–1657, 2010.

[47] Z. Gong, J. Cheng, K. Hu, T. Wang, and L. Wen. An inverse kinematics method of a soft robotic arm with three-dimensional locomotion for underwater manipulation. In *2018 IEEE International Conference on Soft Robotics (RoboSoft)*, pages 516–521. IEEE, 2018.

[48] S. Grazioso, G. Di Gironimo, and B. Siciliano. A geometrically exact model for soft continuum robots: The finite element deformation space formulation. *Soft robotics*, 6(6):790–811, 2019.

[49] C. Guo, X. Li, C. Li, Y. Xu, M. Cai, and X. Xu. A new minimally invasive surgery of hallux valgus: Technique and preliminary outcomes. 2020.

[50] H. Guo, F. Ju, Y. Cao, F. Qi, D. Bai, Y. Wang, and B. Chen. Continuum robot shape estimation using permanent magnets and magnetic sensors. *Sensors and Actuators A: Physical*, 285:519–530, 2019.

[51] R. Hao, E. Erdem Tuna, and M. C. Çavuşoğlu. Contact stability and contact safety of a magnetic resonance imaging-guided robotic catheter under heart surface motion. *Journal of Dynamic Systems, Measurement, and Control*, 143(7), 2021.

[52] R. Hao, T. Greigarn, and M. C. Çavuşoğlu. Contact stability analysis of magnetically-actuated robotic catheter under surface motion. In *2020 IEEE International Conference on Robotics and Automation (ICRA)*, pages 4455–4462. IEEE, 2020.

[53] R. Hao, N. L. Poirot, and M. C. Çavuşoğlu. Analysis of contact stability and contact safety of a robotic intravascular cardiac catheter under blood flow disturbances. In *2020 IEEE/RSJ International Conference on Intelligent Robots and Systems (IROS)*, pages 3216–3223. IEEE, 2020.

[54] Y. He, L. Gao, Y. Bai, H. Zhu, G. Sun, L. Zhu, and H. Xu. Stretchable optical fibre sensor for soft surgical robot shape reconstruction. *Optica Applicata*, 51(4), 2021.

[55] A. Hooshiar, N. M. Bandari, and J. Dargahi. Image-based estimation of contact forces on catheters for robot-assisted cardiovascular intervention. In *Hamlyn Symposium on Medical Robotics*, pages 119–120, 2018.

[56] A. Hooshiar, S. Najarian, and J. Dargahi. Haptic telerobotic cardiovascular intervention: a review of approaches, methods, and future perspectives. *IEEE reviews in biomedical engineering*, 13:32–50, 2019.

[57] A. Hooshiar, A. Sayadi, M. Jolaei, and J. Dargahi. Accurate estimation of tip force on tendon-driven catheters using inverse cosserat rod model. In *2020 International Conference on Biomedical Innovations and Applications (BIA)*, pages 37–40. IEEE, 2020.

[58] A. Hooshiar, A. Sayadi, M. Jolaei, and J. Dargahi. Analytical tip force estimation on tendon-driven catheters through inverse solution of cosserat rod model. In *2021 IEEE/RSJ International Conference on Intelligent Robots and Systems (IROS)*, pages 1829–1834. IEEE, 2021.

[59] B. N. G. I. Isbister, A. An integrated kinematic modeling and experimental approach for an active endoscope. *Front. Robot. AI*, 8, 2021.

[60] M. Ji, Q. Li, I. H. Cho, and J. Kim. Rapid design and analysis of microtube pneumatic actuators using line-segment and multi-segment euler–bernoulli beam models. *Micromachines*, 10(11):780, 2019.

[61] A. S. John, I. Caturegli, N. S. Kubicki, and S. M. Kavic. The rise of minimally invasive surgery: 16 year analysis of the progressive replacement of open surgery with laparoscopy. *JSLS: Journal of the Society of Laparoscopic & Robotic Surgeons*, 24(4), 2020.

[62] M. Jolaei, A. Hooshiar, and J. Dargahi. Displacement-based model for estimation of contact force between rfa catheter and atrial tissue with ex-vivo validation. In *2019 IEEE International Symposium on Robotic and Sensors Environments (ROSE)*, pages 1–7. IEEE, 2019.

[63] M. T. Kanada, A. Switching between continuum and discrete states in a continuum robot with dislocatable joints. *IEEE Access*, 9:34859–34867, 2021.

[64] R. Khoshbakht, M. Kheiri, J. Dargahi, and A. Hooshiar. Effects of blood flow on the tip contact force of cardiac ablation catheters. In *2022 IEEE International Symposium on Robotic and Sensors Environments (ROSE)*, pages 1–7. IEEE, 2022.

[65] Y. Kim, G. A. Parada, S. Liu, and X. Zhao. Ferromagnetic soft continuum robots. *Science Robotics*, 4(33):eaax7329, 2019.

[66] B. P. Krijthe, A. Kunst, E. J. Benjamin, G. Y. Lip, O. H. Franco, A. Hofman, J. C. Witteman, B. H. Stricker, and J. Heeringa. Projections on the number of individuals

with atrial fibrillation in the european union, from 2000 to 2060. *European heart journal*, 34(35):2746–2751, 2013.

[67] T. Küffer, A. Haeberlin, S. Knecht, S. H. Baldinger, A. Madaffari, J. Seiler, A. Mühl, H. Tanner, L. Roten, and T. Reichlin. Validation of the accuracy of contact force measurement by contemporary force-sensing ablation catheters. *Journal of cardiovascular electrophysiology*, 34(2):292–299, 2023.

[68] T. Kurmann, P. Marquez Neila, X. Du, P. Fua, D. Stoyanov, S. Wolf, and R. Sznitman. Simultaneous recognition and pose estimation of instruments in minimally invasive surgery. In *Medical Image Computing and Computer-Assisted Intervention- MICCAI 2017: 20th International Conference, Quebec City, QC, Canada, September 11-13, 2017, Proceedings, Part II 20*, pages 505–513. Springer, 2017.

[69] N. Lang, M. J. Pereira, Y. Lee, I. Friehs, N. V. Vasilyev, E. N. Feins, K. Ablasser, E. D. O'Cearbhaill, C. Xu, A. Fabozzo, et al. A blood-resistant surgical glue for minimally invasive repair of vessels and heart defects. *Science translational medicine*, 6(218):218ra6–218ra6, 2014.

[70] J. Lantz, V. Gupta, L. Henriksson, M. Karlsson, A. Persson, C.-J. Carlhäll, and T. Ebbers. Impact of pulmonary venous inflow on cardiac flow simulations: comparison with in vivo 4d flow mri. *Annals of biomedical engineering*, 47:413–424, 2019.

[71] K. Lee. Large deflections of cantilever beams of non-linear elastic material under a combined loading. *International Journal of Non-Linear Mechanics*, 37(3):439–443, 2002.

[72] M. Lerotic and G.-Z. Yang. The use of super resolution in robotic assisted minimally

invasive surgery. In *Medical Image Computing and Computer-Assisted Intervention–MICCAI 2006: 9th International Conference, Copenhagen, Denmark, October 1-6, 2006. Proceedings, Part I 9*, pages 462–469. Springer, 2006.

[73] K. Li, F. Liu, P. Liu, C. Wei, X. Li, et al. Clinical effect and aesthetic evaluation of minimally invasive implant therapy. *Emergency Medicine International*, 2023, 2023.

[74] L. Li, T. Jin, Y. Tian, F. Yang, and F. Xi. Design and analysis of a square-shaped continuum robot with better grasping ability. *IEEE Access*, 7:57151–57162, 2019.

[75] M. Liévin and E. Keeve. Stereoscopic augmented reality system for computer-assisted surgery. In *International Congress Series*, volume 1230, pages 107–111. Elsevier, 2001.

[76] G. Lippi, F. Sanchis-Gomar, and G. Cervellin. Global epidemiology of atrial fibrillation: an increasing epidemic and public health challenge. *International Journal of Stroke*, 16(2):217–221, 2021.

[77] P. Lloyd, Z. Koszowska, M. Di Lecce, O. Onaizah, J. H. Chandler, and P. Valdastri. Feasibility of fiber reinforcement within magnetically actuated soft continuum robots. *Frontiers in Robotics and AI*, 8:715662, 2021.

[78] Y. Lou, T. Yang, D. Luo, J. Wu, and Y. Dong. A novel catheter distal contact force sensing for cardiac ablation based on fiber bragg grating with temperature compensation. *Sensors*, 23(5):2866, 2023.

[79] G. Mariani, L. Bruselli, T. Kuwert, E. E. Kim, A. Flotats, O. Israel, M. Dondi, and N. Watanabe. A review on the clinical uses of spect/ct. *European journal of nuclear medicine and molecular imaging*, 37:1959–1985, 2010.

[80] A. Mate. The frenet-serret formulas. *Brooklyn Collage Of The City University Of New York, izdano*, 19, 2017.

[81] H. Nakagawa and W. M. Jackman. The role of contact force in atrial fibrillation ablation. *Journal of atrial fibrillation*, 7(1), 2014.

[82] N. Naughton, J. Sun, A. Tekinalp, T. Parthasarathy, G. Chowdhary, and M. Gazzola. Elastica: A compliant mechanics environment for soft robotic control. *IEEE Robotics and Automation Letters*, 6(2):3389–3396, 2021.

[83] R. M. Neal. *Bayesian learning for neural networks*, volume 118. Springer Science & Business Media, 2012.

[84] J. Negrillo-Cárdenas, J.-R. Jiménez-Pérez, J. Madeira, and F. R. Feito. A virtual reality simulator for training the surgical reduction of patient-specific supracondylar humerus fractures. *International Journal of Computer Assisted Radiology and Surgery*, 17(1):65–73, 2022.

[85] G. Olson, R. L. Hatton, J. A. Adams, and Y. Mengüç. An euler–bernoulli beam model for soft robot arms bent through self-stress and external loads. *International Journal of Solids and Structures*, 207:113–131, 2020.

[86] A. Omran, A. A. Arifi, and A. Mohamed. Echocardiography in mitral stenosis. *Journal of the Saudi heart Association*, 23(1):51–58, 2011.

[87] D. Padmanabhan, P. S. M. Rao, H. J. Pandya, et al. Force sensing technologies for catheter ablation procedures. *Mechatronics*, 64:102295, 2019.

[88] L. Pancaldi, L. Noseda, A. Dolev, A. Fanelli, D. Ghezzi, A. J. Petruska, and M. S.

Sakar. Locomotion of sensor-integrated soft robotic devices inside sub-millimeter arteries with impaired flow conditions. *Advanced Intelligent Systems*, 4(5):2100247, 2022.

[89] A. Parisi, D. Reim, F. Borghi, N. T. Nguyen, F. Qi, A. Coratti, F. Cianchi, M. Cesari, F. Bazzocchi, O. Alimoglu, et al. Minimally invasive surgery for gastric cancer: A comparison between robotic, laparoscopic and open surgery. *World journal of gastroenterology*, 23(13):2376, 2017.

[90] T. Pfaff, M. Fortunato, A. Sanchez-Gonzalez, and P. W. Battaglia. Learning mesh-based simulation with graph networks. *arXiv preprint arXiv:2010.03409*, 2020.

[91] P. Polygerinos, T. Schaeffter, L. Seneviratne, and K. Althoefer. A fibre-optic catheter-tip force sensor with mri compatibility: A feasibility study. In *2009 Annual International Conference of the IEEE Engineering in Medicine and Biology Society*, pages 1501–1054. IEEE, 2009.

[92] F. Qi, F. Ju, D. Bai, Y. Wang, and B. Chen. Kinematic analysis and navigation method of a cable-driven continuum robot used for minimally invasive surgery. *The International Journal of Medical Robotics and Computer Assisted Surgery*, 15(4):e2007, 2019.

[93] K. Rajappan and M. Ginks. Catheter ablation of persistent atrial fibrillation. *Future Cardiology*, 10(4):553–562, 2014.

[94] T. Reichlin, S. H. Baldinger, E. Pruvot, L. Bisch, P. Ammann, D. Altmann, B. Berte, R. Kobza, L. Haegeli, C. Schlatzer, et al. Impact of contact force sensing technology on outcome of catheter ablation of idiopathic pre-mature ventricular contractions originating from the outflow tracts. *EP Europace*, 23(4):603–609, 2021.

[95] Z. Ren, R. Zhang, R. H. Soon, Z. Liu, W. Hu, P. R. Onck, and M. Sitti. Soft-bodied adaptive multimodal locomotion strategies in fluid-filled confined spaces. *Science advances*, 7(27):eabh2022, 2021.

[96] R. Richa, A. P. Bó, and P. Poignet. Robust 3d visual tracking for robotic-assisted cardiac interventions. In *Medical Image Computing and Computer-Assisted Intervention–MICCAI 2010: 13th International Conference, Beijing, China, September 20-24, 2010, Proceedings, Part I 13*, pages 267–274. Springer, 2010.

[97] R. J. Roesthuis and S. Misra. Steering of multisegment continuum manipulators using rigid-link modeling and fbg-based shape sensing. *IEEE transactions on robotics*, 32(2):372–382, 2016.

[98] G. Runge, M. Wiese, L. Günther, and A. Raatz. A framework for the kinematic modeling of soft material robots combining finite element analysis and piecewise constant curvature kinematics. In *2017 3rd International Conference on Control, Automation and Robotics (ICCAR)*, pages 7–14. IEEE, 2017.

[99] S. K. Sahu, C. Sozer, B. Rosa, I. Tamadon, P. Renaud, and A. Menciassi. Shape reconstruction processes for interventional application devices: State of the art, progress, and future directions. *Frontiers in Robotics and AI*, 8:758411, 2021.

[100] R. Sanchez-Matilla, M. Robu, I. Luengo, and D. Stoyanov. Scalable joint detection and segmentation of surgical instruments with weak supervision. In *International Conference on Medical Image Computing and Computer-Assisted Intervention*, pages 501–511. Springer, 2021.

[101] A. Sayadi, H. R. Nourani, M. Jolaei, J. Dargahi, and A. Hooshiar. Force estimation on

steerable catheters through learning-from-simulation with ex-vivo validation. In *2021 International Symposium on Medical Robotics (ISMR)*, pages 1–6. IEEE, 2021.

[102] A. Sayadi, H. R. Nourani, M. Jolaei, J. Dargahi, and A. Hooshiar. Force estimation on steerable catheters through learning-from-simulation with ex-vivo validation. In *2021 International Symposium on Medical Robotics (ISMR)*, pages 1–6. IEEE, 2021.

[103] C. Semler, G. X. Li, and M. Paıdoussis. The non-linear equations of motion of pipes conveying fluid. *Journal of Sound and Vibration*, 169(5):577–599, 1994.

[104] I. S. Shchelik, J. V. Molino, and K. Gademann. Biohybrid microswimmers against bacterial infections. *Acta Biomaterialia*, 136:99–110, 2021.

[105] J. Shi, J. C. Frantz, A. Shariati, A. Shiva, J. S. Dai, D. Martins, and H. A. Wurdemann. Screw theory-based stiffness analysis for a fluidic-driven soft robotic manipulator. In *2021 IEEE International Conference on Robotics and Automation (ICRA)*, pages 11938–11944. IEEE, 2021.

[106] H. R. Shin, K. Lee, H. W. Yu, S.-j. Kim, Y. J. Chai, J. Y. Choi, and K. E. Lee. Comparison of perioperative outcomes using the da vinci s, si, x, and xi robotic platforms for baba robotic thyroidectomy. *Medicina*, 57(10):1130, 2021.

[107] J. So, U. Kim, Y. B. Kim, D.-Y. Seok, S. Y. Yang, K. Kim, J. H. Park, S. T. Hwang, Y. J. Gong, and H. R. Choi. Shape estimation of soft manipulator using stretchable sensor. *Cyborg and Bionic Systems*, 2021.

[108] C. Song. History and current situation of shape memory alloys devices for minimally invasive surgery. *TOMDJ*, 2:24–31, 2010.

[109] S. Song, C. Zhang, L. Liu, and M. Q.-H. Meng. Preliminary study on magnetic tracking-based planar shape sensing and navigation for flexible surgical robots in transoral surgery: methods and phantom experiments. *International journal of computer assisted radiology and surgery*, 13:241–251, 2018.

[110] M. Sun, C. Tian, L. Mao, X. Meng, X. Shen, B. Hao, X. Wang, H. Xie, and L. Zhang. Reconfigurable magnetic slime robot: deformation, adaptability, and multifunction. *Advanced Functional Materials*, 32(26):2112508, 2022.

[111] S. S. Tabatabaei, M. Kheiri, and J. Dargahi. Dynamics and stability of imperfect flexible cylinders in axial flow. *Journal of Fluids and Structures*, 105:103321, 2021.

[112] K. Takashima, R. Shimomura, T. Kitou, H. Terada, K. Yoshinaka, and K. Ikeuchi. Contact and friction between catheter and blood vessel. *Tribology International*, 40(2):319–328, 2007.

[113] J. Thiboutot, A. C. Argento, J. Akulian, H. J. Lee, A. DeMaio, C. M. Kapp, M. M. Wahidi, and L. Yarmus. Accuracy of pulmonary nodule sampling using robotic assisted bronchoscopy with shape sensing, fluoroscopy, and radial endobronchial ultrasound (the accuracy study). *Respiration*, 101(5):485–493, 2022.

[114] T. G. Thuruthel, E. Falotico, M. Cianchetti, F. Renda, and C. Laschi. Learning global inverse statics solution for a redundant soft robot. In *Proceedings of the 13th International Conference on Informatics in Control, Automation and Robotics*, volume 2, pages 303–310, 2016.

[115] T. G. Thuruthel, E. Falotico, F. Renda, and C. Laschi. Model-based reinforcement learning for closed-loop dynamic control of soft robotic manipulators. *IEEE Transactions on Robotics*, 35(1):124–134, 2018.

[116] J. Tian, K. O. Afebu, Z. Wang, Y. Liu, and S. Prasad. Dynamic analysis of a soft capsule robot self-propelling in the small intestine via finite element method. *Nonlinear Dynamics*, 111(11):9777–9798, 2023.

[117] J. Till, V. Aloi, and C. Rucker. Real-time dynamics of soft and continuum robots based on cosserat rod models. *The International Journal of Robotics Research*, 38(6):723–746, 2019.

[118] T. Torkaman, M. Roshanfar, J. Dargahi, and A. Hooshiar. Analytical modeling and experimental validation of a gelatin-based shape sensor for soft robots. In *2022 International Symposium on Medical Robotics (ISMR)*, pages 1–7. IEEE, 2022.

[119] V. K. Venkiteswaran, J. Sikorski, and S. Misra. Shape and contact force estimation of continuum manipulators using pseudo rigid body models. *Mechanism and machine theory*, 139:34–45, 2019.

[120] E. Vignali, E. Gasparotti, K. Capellini, B. M. Fanni, L. Landini, V. Positano, and S. Celi. Modeling biomechanical interaction between soft tissue and soft robotic instruments: importance of constitutive anisotropic hyperelastic formulations. *The International Journal of Robotics Research*, 40(1):224–235, 2021.

[121] C. Wang, Y. Wu, X. Dong, M. Armacki, and M. Sitti. In situ sensing physiological properties of biological tissues using wireless miniature soft robots. *Science advances*, 9(23):eadg3988, 2023.

[122] H. Wang, M. Totaro, and L. Beccai. Toward perceptive soft robots: Progress and challenges. *Advanced Science*, 5(9):1800541, 2018.

[123] P. Wang, S. Zhang, Z. Liu, Y. Huang, J. Huang, X. Huang, J. Chen, B. Fang, and

D. Peng. Smart laparoscopic grasper integrated with fiber bragg grating based tactile sensor for real-time force feedback. *Journal of Biophotonics*, 15(5):e202100331, 2022.

[124] X.-Q. Wang, Y. Design and fabrication of a new dual-arm soft robotic manipulator. *Actuators*, 8:5, 2019.

[125] I. Waters, D. Jones, A. Alazmani, and P. Culmer. Encouraging and detecting preferential incipient slip for use in slip prevention in robot-assisted surgery. *Sensors*, 22(20):7956, 2022.

[126] A. Wutzler, T. Wolber, W. Haverkamp, and L.-H. Boldt. Robotic ablation of atrial fibrillation. *JoVE (Journal of Visualized Experiments)*, (99):e52560, 2015.

[127] N. Xia, G. Zhu, X. Wang, Y. Dong, and L. Zhang. Multicomponent and multifunctional integrated miniature soft robots. *Soft Matter*, 18(39):7464–7485, 2022.

[128] R. Xu, A. Yurkewich, and R. V. Patel. Curvature, torsion, and force sensing in continuum robots using helically wrapped fbg sensors. *IEEE Robotics and Automation Letters*, 1(2):1052–1059, 2016.

[129] W. Xu, M. Auli, and S. Clark. Ccg supertagging with a recurrent neural network. In *Proceedings of the 53rd Annual Meeting of the Association for Computational Linguistics and the 7th International Joint Conference on Natural Language Processing (Volume 2: Short Papers)*, pages 250–255, 2015.

[130] H. Z. Yang, E. S. Clinical comparison of 3 different double eyelid surgeries. *Ann Plast Surg*, 88:138–143, 2021.

[131] H. Yuan, P. W. Y. Chiu, and Z. Li. Shape-reconstruction-based force sensing method

for continuum surgical robots with large deformation. *IEEE Robotics and Automation Letters*, 2(4):1972–1979, 2017.

[132] X. Zhang, M. Du, J. Zhang, and H. Li. Application of digital minimally invasive medicine and visual simulation in surgery. In *7th International Conference on Management, Education, Information and Control (MEICI 2017)*, pages 873–876. Atlantis Press, 2017.

[133] X. Zhang, J. Kow, D. Jones, G. de Boer, A. Ghanbari, A. Serjouei, P. Culmer, and A. Alazmani. Adjustable compliance soft sensor via an elastically inflatable fluidic dome. *Sensors*, 21(6):1970, 2021.

[134] H. Zhao, J. Jalving, R. Huang, R. Knepper, A. Ruina, and R. Shepherd. A helping hand: Soft orthosis with integrated optical strain sensors and emg control. *IEEE Robotics & Automation Magazine*, 23(3):55–64, 2016.